Obesogenic High-Fat Diet and MYC Cooperate to Promote Lactate Accumulation and Tumor Microenvironment Remodeling in Prostate Cancer

Nadia Boufaied[1], Paolo Chetta[2,3], Tarek Hallal[1,4], Stefano Cacciatore[5], Daniela Lalli[6], Carole Luthold[7], Kevin Homsy[7], Eddie L. Imada[8], Sudeepa Syamala[9], Cornelia Photopoulos[9], Anna Di Matteo[10], Anna de Polo[1], Alessandra Maria Storaci[11], Ying Huang[9], Francesca Giunchi[12], Patricia A. Sheridan[13], Gregory Michelotti[13], Quang-De Nguyen[14], Xin Zhao[15], Yang Liu[15], Elai Davicioni[15], Daniel E. Spratt[16], Simone Sabbioneda[10], Giovanni Maga[10], Lorelei A. Mucci[17], Claudia Ghigna[10], Luigi Marchionni[8], Lisa M. Butler[18], Leigh Ellis[19], François Bordeleau[7,20], Massimo Loda[8], Valentina Vaira[11,21], David P. Labbé[1,4,22], and Giorgia Zadra[9,10,23]

ABSTRACT

Cancer cells exhibit metabolic plasticity to meet oncogene-driven dependencies while coping with nutrient availability. A better understanding of how systemic metabolism impacts the accumulation of metabolites that reprogram the tumor microenvironment (TME) and drive cancer could facilitate development of precision nutrition approaches. Using the Hi-MYC prostate cancer mouse model, we demonstrated that an obesogenic high-fat diet (HFD) rich in saturated fats accelerates the development of c-MYC–driven invasive prostate cancer through metabolic rewiring. Although c-MYC modulated key metabolic pathways, interaction with an obesogenic HFD was necessary to induce glycolysis and lactate accumulation in tumors. These metabolic changes were associated with augmented infiltration of $CD206^+$ and $PD\text{-}L1^+$ tumor-associated macrophages (TAM) and $FOXP3^+$ regulatory T cells, as well as with the activation of transcriptional programs linked to disease progression and therapy resistance. Lactate itself also stimulated neoangiogenesis and prostate cancer cell migration, which were significantly reduced following treatment with the lactate dehydrogenase inhibitor FX11. In patients with prostate cancer, high saturated fat intake and increased body mass index were associated with tumor glycolytic features that promote the infiltration of M2-like TAMs. Finally, upregulation of lactate dehydrogenase, indicative of a lactagenic phenotype, was associated with a shorter time to biochemical recurrence in independent clinical cohorts. This work identifies cooperation between genetic drivers and systemic metabolism to hijack the TME and promote prostate cancer progression through oncometabolite accumulation. This sets the stage for the assessment of lactate as a prognostic biomarker and supports strategies of dietary intervention and direct lactagenesis blockade in treating advanced prostate cancer.

Significance: Lactate accumulation driven by high-fat diet and MYC reprograms the tumor microenvironment and promotes prostate cancer progression, supporting the potential of lactate as a biomarker and therapeutic target in prostate cancer.

See related commentary by Frigo, p. 1742

[1]Cancer Research Program, Research Institute of the McGill University Health Centre, Montréal, Québec, Canada. [2]University of Milan, Residency Program in Pathology, Milan, Italy. [3]Department of Pathology, Massachusetts General Hospital, Boston, Massachusetts. [4]Department of Anatomy and Cell Biology, McGill University, Montréal, Québec, Canada. [5]Bionformatics Unit, International Centre for Genetic Engineering and Biotechnology (ICGEB), Cape Town, South Africa. [6]Department of Science and Technological Innovation, University of Piemonte Orientale "A. Avogadro," Alessandria, Italy. [7]CHU de Québec-Université Laval Research Center (Oncology Division) and Cancer Research Center, Centre de Recherche en Organogénèse Expérimentale/LOEX, Université Laval, Québec, Canada. [8]Department of Pathology and Laboratory Medicine, Weill Cornell Medicine, New York Presbyterian-Weill Cornell Campus, New York, New York. [9]Department of Oncologic Pathology, Dana-Farber Cancer Institute, Harvard Medical School, Boston, Massachusetts. [10]Institute of Molecular Genetics, National Research Council (CNR-IGM), Pavia, Italy. [11]Department of Pathophysiology and Transplantation, University of Milan, Milan, Italy. [12]Pathology Unit, IRCCS Azienda Ospedaliero-Universitaria di Bologna, Bologna, Italy. [13]Metabolon Inc., Morrisville, North Carolina. [14]Department of Imaging, Lurie Family Imaging Center, Center for Biomedical Imaging in Oncology, Dana-Farber Cancer Institute, Harvard Medical School, Boston, Massachusetts. [15]Veracyte, South San Francisco, California. [16]Department of Radiation Oncology, University Hospitals Seidman Cancer Center, Case Western Reserve University School of Medicine, Cleveland, Ohio. [17]Department of Epidemiology, Harvard T.H. Chan School of Public Health, Boston, Massachusetts. [18]South Australian Immunogenomics Cancer Institute and Freemasons Centre for Male Health and Wellbeing, University of Adelaide, South Australian Health and Medical Research Institute, Adelaide, Australia. [19]Department of Surgery, Center for Prostate Disease Research, Murtha Cancer Center Research Program, Uniformed Services University of the Health Sciences and the Walter Reed National Military Medical Center; The Henry M. Jackson Foundation for the Advancement of Military Medicine, Inc., Bethesda, Maryland. [20]Department of Molecular Biology, Clinical Biochemistry, and Pathology, Laval University, Québec, Canada. [21]Division of Pathology, Fondazione IRCCS Ca' Granda Ospedale Maggiore Policlinico, Milan, Italy. [22]Division of Urology, Department of Surgery, McGill University, Montréal, Québec, Canada. [23]Department of Pathology, Brigham and Women's Hospital, Harvard Medical School, Boston, Massachusetts.

N. Boufaied and P. Chetta contributed equally as co-first authors of this article.

D.P. Labbé and G. Zadra contributed equally as co-senior authors of this article.

Current address for P. Chetta: Department of Pathology, Massachusetts General Hospital, Boston, MA; current address for C. Photopoulos: Beth Israel Deaconess Medical Center, Harvard Medical School, Cambridge, MA; current address for A. de Polo: Center for Genomic Science of IIT@SEMM, Italian Institute of Technology, Milan, Italy; current address for Y. Huang: Novartis Institutes for BioMedical Research (NIBR), Cambridge, MA; and current address for G. Zadra: Institute of Molecular Genetics, National Research Council (CNR-IGM), Pavia, Italy.

Corresponding Authors: David P. Labbé, McGill University, Research Institute of the McGill University Health Centre, Montréal, Québec H4A 3J1, Canada. E-mail: david.labbe@mcgill.ca; and Giorgia Zadra (lead contact), Institute of Molecular Genetics, National Research Council, Pavia, 27100, Italy. E-mail: giorgia.zadra@cnr.it

Cancer Res 2024;84:1834–55

doi: 10.1158/0008-5472.CAN-23-0519

Introduction

Western society is experiencing widespread consumption of saturated fat- and sugar-rich food and increasing rates of obesity (1). Obesity is a putative major risk factor for at least 13 cancer types and may soon overtake smoking in the ranking of preventable cancer risk factors (2). Understanding of the molecular mechanisms linking the consumption of unhealthy diets and/or obesity to cancer incidence/progression has therefore become a priority (3). Experimental and clinical studies have endorsed caloric restriction and weight management as strategies to reduce cancer advancement and improve treatment outcomes (4, 5). Because caloric restriction regimens may not be sustainable in the long run, intermittent fasting–mimicking diets are currently under investigation with promising results in the clinic (6, 7). Still, new approaches of precision nutrition and/or *ad hoc* pharmacological modulation of cancer-driven metabolic pathways are sorely needed. Metabolites such as lactate, kynurenine, and arginine have recently emerged as key mediators of tumor/tumor microenvironment (TME) cross-talk, immune evasion, and resistance to therapies (8, 9). However, whether perturbations in systemic metabolism support the intratumoral accumulation of metabolites that shape TME and promote cancer progression is still an open question. Prostate cancer is the second cause of cancer-related death in men in the United States, and the third in Europe (10, 11). Obesity status, lifestyle, and environmental factors, including diet, profoundly affect the course of the disease (12). Although the association between obesity and worse prostate cancer progression/lethality is well established (13), the link between increased consumption of saturated fatty acids (FA) and fatal prostate cancer is still the object of debate (14). Our group has previously demonstrated that a lard-based obesogenic high-fat diet (HFD) promotes alterations of one-carbon metabolism [i.e., s-adenosylhomocysteine (SAH) levels] in prostate intraepithelial neoplasia (PIN), precursor of invasive adenocarcinoma (IA). Increased SAH was associated with the demethylation of the H4K20 histone mark and amplification of a c-MYC transcriptional program, suggesting obesogenic HFD-mediated reprogramming of the metabolic/epigenetic axis at an early stage in the disease process (15). The oncogene c-MYC (MYC) is overexpressed and amplified in many human malignancies, including prostate cancer (16). MYC still remains a challenging target, calling for a better understanding of druggable metabolic vulnerabilities driven by MYC (17). In the Hi-MYC transgenic model, at 24 weeks, MYC consistently drives the transition from PIN to IA, which faithfully resembles the human disease (18). Here, we leveraged the Hi-MYC model to investigate the underpinning mechanisms that foster late prostate cancer progression under a prolonged exposure to obesogenic HFD. Integrating digital pathology, transcriptomics, metabolomics, and computational analyses, our study uncovers a concerted cooperation between obesogenic HFD and MYC genetic drive to remodel the TME, promote immunosurveillance escape, and sustain prostate cancer progression through a metabolic switch toward glycolysis and accumulation of the oncometabolite lactate.

Materials and Methods

Cell lines and reagents

MYC-CaP cells were authenticated and purchased from the ATCC (#CRL-3255, RRID:CVCL_J703). Method of authentication at the ATCC is STR profiling. Cells were used at early passages (p3-p8) and kept in culture longer for migration experiments (p18-p24). Immortalized HUVEC/TERT2 (#CHT-006–0008, RRID:CVCL_9Q53) cells were authenticated and purchased from Evercyte GmbH. Method of authentication at Evercyte GmbH is STR profiling. Cells tested negative for *Mycoplasma* during the entire study (MycoAlert *Mycoplasma* Detection Kit, Lonza, #LT07–418). MYC-CaP cells were grown in DMEM high-glucose (Gibco, #11965118 or Euroclone, #ECM0728L, #ECB7501L) with 10% FBS (Gibco, #10270106), 100 U/mL penicillin, and 0.1 mg/mL streptomycin (Gibco, #15140122 or Euroclone, #ECB300ID), 4 mmol/L glutamine (Gibco, #25030081 or Euroclone, #ECB3000D). DMEM low-glucose (Euroclone, #ECM0749L) or XF DMEM pH 7.4 (Agilent Technologies, #103575–100) were used for selected experiments, as indicated. Physiological medium was defined as XF DMEM pH 7.4 with addition of 5 mmol/L glucose, 0.5 mmol/L glutamine, and 150 μmol/L pyruvate. HUVEC cells were grown according to supplier instructions in 10% FBS EBM basal medium (Lonza, #CC-3156) with selected supplements (BBE, HEGF, hydrocortisone solution, and ascorbic acid solution) from EGM SingleQuot Kit (Lonza, #CC-4133) and 20 μg/mL Geneticin (Gibco, #10131–019). A protein lysate from HeLa cells (purchased at ATCC, #CCL-2, RRID: CVCL_0030) was used as positive control for western blotting experiments. HeLa cells were grown in standard conditions [DMEM high-glucose (Euroclone, #ECB7501L) supplemented with 10% FBS (Euroclone, #ECS 0180L), 4 mmol/L L-glutamine (Euroclone, #ECB3000D), 100 U/mL penicillin/0.1 mg/mL streptomycin (Euroclone, #ECB300ID). Lactate (Sigma-Aldrich, #L-7022), lactate dehydrogenase (LDHA) inhibitor FX11 (Calbiochem, #EMD 427218), and monocarboxylate transporters 1 and 4 (MCT-1/MCT-4) dual inhibitor syrosingopine (Sigma-Aldrich, #SML1908) were diluted in PBS and DMSO, respectively.

Preclinical models and *in vivo* imaging

Hi-MYC mice (FVB-Tg(ARR2/Pbsn-MYC)7Key/Nci, strain number 01XK8, RRID:IMSR_NCIMR:01XK8), expressing the human c-MYC transgene in prostatic epithelium (18), were obtained from the National Cancer Institute Mouse Repository at Frederick National Laboratory for Cancer Research and housed at the Dana-Farber Cancer Institute (DFCI) Animal Resources Facility. Upon weaning (3 weeks of age), heterozygous male mice and their wild-type littermates (WT) were fed a purified control diet (CTD; 10% fat, Harlan Laboratories, TD.130838) or an HFD (60% fat, Harlan Laboratories, #TD.06414) for 21 weeks as described previously (15). The two diets were carefully designed to modulate caloric intake from fat while keeping caloric intake from protein constant. Food was changed on a weekly basis. Mice were weighed every three weeks and before euthanasia. Animals were kept on a 12-hour light/dark cycle and allowed free access to food and water. Mice were euthanized by CO_2, followed by cervical dislocation. Blood was collected by cardiac puncture; serum was obtained using serum-separating tubes (Sarstedt, #41.1378.005) and stored at −80°C. Upon collection, urogenital apparatus and liver tissues were fixed in 10% formalin (Sakura, #5993) and embedded in paraffin. Alternatively, prostate lobes (anterior, AP; ventral, VP; dorsolateral, DLP) were dissected under a stereomicroscope, weighed, and flash-frozen in liquid nitrogen. Serum and tissues were harvested in the morning to minimize inter-sample and circadian rhythm variability. 2-deoxy-2-[^{18}F] fluoro-D-glucose (^{18}F-FDG) *in vivo* imaging was performed in MYC-CaP allografts from FVB mice fed an HFD or CTD (n = 9/diet; imaged = 5/diet) using a dedicated small animal scanner (Inveon Multimodality System, Siemens Medical Solutions USA, Inc.). Briefly, eighteen 3-week-old FVB male mice were bought from the Charles River Laboratories. Mice were weighted and randomly assigned to CTD or HFD, monitored daily, and weighted once/week. Researchers were not blind to diet conditions. After 34 days, mice were injected with *Mycoplasma*-free

MYC-CaP cells p3 (1×10^6 in PBS: Matrigel, 1:1). Tumor formation and mouse weight were monitored weekly. Three weeks later, 5 mice/group were selected for *in vivo* imaging (tumor volume >100 mm^3 measured by caliper). 2-deoxy-2-[^{18}F] fluoro-D-glucose (^{18}F-FDG) PET imaging was carried out on a dedicated small animal scanner (Inveon Multimodality System, Siemens Medical Solutions USA, Inc.). One hour before radiotracer administration, mice were warmed on Gaymar circulating warm water heating pads to reduce brown fat uptake and anesthetized through sevoflurane/air inhalation. Mice were injected with a bolus intravenous injection (through the lateral tail vein) of approximately 7.4 MBq of ^{18}F-FDG (PETNet SolutionsA) and remained under anesthesia throughout the 60 minutes uptake period. Mice were subsequently placed into the scanner. Static PET emission scans were acquired in list-mode format over 10 minutes and corrected for decay and dead time. A low-dose CT scans was then acquired (80 kVp, 0.5 mA) for anatomical reference and to provide guidance for the delineation of selected tissue volume of interest (VOI). Acquired data were then sorted into 0.5-mm sinogram bins and 1-time frame for image reconstruction using FORE/3D-OSEM-MAP image reconstruction. Reconstructed PET/CT images were analyzed with the Siemens Inveon Research Workplace software. Radioactivity retention within the selected VOI was obtained from mean voxel intensity values within the VOI and then converted to megabecquerels per milliliter using the calibration factor determined for the Inveon PET System. These values were then divided by the administered activity dose and mouse body weight to obtain an image VOI-derived standardized uptake value (SUV). Both mean and maximum SUV value (SUVmean and SUVmax) within a VOI were used as quantitative imaging metrics. One mouse form HFD group was removed from the analysis due to non-suitable tumor volume for PET imaging, revealed by CT. Imaging was performed at the Lurie Family Imaging Center, DFCI. Animal studies were reviewed and approved by the DFCI Institutial Care and Use Committee (IACUC; approved protocols #13–049; #08–023), and were in accordance with the Animal Welfare Act and ARRIVE guidelines. Sample size for PET imaging, metabolomics, and RNA-sequencing (RNA-seq) experiments was determined on the basis of our and other previous publications in line with conventional recommendations (15, 19).

IHC

Paraffin-embedded murine tissues were sectioned into 5-μm slices, deparaffinized, rehydrated, and stained with hematoxylin and eosin (H&E). Consecutive sections of prostatic tissues were stained with anti–Ki-67 mAb (Vector Laboratories, # VP-RM04, RRID: AB_2336545, dilution 1:250, Bond III staining platform), anti-smooth muscle α-actin mAb (Cell Signaling Technology, CST; #19245, clone: D4K9N, RRID:AB_2734735, dilution 1:500, Bond Polymer Refine Kit in Leica Bond RX system) or anti-FOXP3 mAb (R&D Systems, #MAB8214, clone:1054C, RRID:AB_2929004, dilution 1:100, Ventana BenchMark ULTRA system), following manufacturer instructions. Ki-67 staining and analysis was performed as described in ref. 15. The percentage of Ki-67+ cells was determined by a board-certified MD Pathologist (F.G.) by counting the tumor cells that are positive for nuclear Ki-67 as a function of the total number of tumor cells in ten high-power fields. For F4/80 and CD260 dual IHC staining, tissue sections were first incubated with anti-F4/80 mAb (CST, #70076S, RRID:AB_2799771, dilution 1:300) followed by incubation with the Discovery OmniMap anti-Rb-HRP secondary antibody (Roche, #760–4311, RRID:AB_2811043) and signal detection with Discovery Teal HRP detection Kit (Roche, #760–247). Following antibodies denaturation, sections were re-incubated with anti-CD206 (CST, #24595, RRID:AB_2892682, dilution: 1:4,000). Second signal was detected with Discovery Yellow detection kit (Roche, #760–250). Slides were then counterstained with hematoxylin, dehydrated, cleared and coverslipped. F4/80$^+$ CD206$^+$ cells were counted using the open-source software QuPath (RRID:SCR_018257, version 0.4.4) by a board-certified MD Pathologist (P.C.). Pathologists were blind to diet/genotype conditions. For all tissue slides, images were acquired using Aperio (Leica) or Perkin Elmer Vectra 3 (PerkinElmer, Inc.) or Nano Zoomer-XR (Hamamatsu) image scanner systems. Sample size was calculated with the software G*power version 3.1 (RRID: SCR_013726). On the basis of Blando and colleagues (20), we determined that 20–25 mice/group were adequate to detect a significant difference in IA incidence with an effect size of about 0.4, α-error of 0.05, and power of 0.80.

Imaging analysis

For the definition of PIN percentage and invasive areas, imaging analysis was carried out on H&E-stained slides with the support of the HALO software (licensed, Indica Labs). A board-certified MD pathologist (P. Chetta), blinded to experimental conditions, manually segmented each scanned tissue slide into AP, VP, and DLP annotation layers. A separate annotation layer was drawn for IA whenever applicable. Similar to Gertych and colleagues (21), random forests-based classification systems were trained to identify atypical epithelium, benign epithelium, stroma, glandular lumen, and background. IA layers were digitally classified into adenocarcinoma, stroma, and background. The atypical epithelium category served as a morphological surrogate for a diagnosis of PIN. The output of each digital classification was carefully reviewed by P. Chetta and edited as necessary. The surface area for each tissue category/annotation layer was digitally quantified. The Fisher exact test was used to determine the association between HFD and invasive phenotype. FOXP3 was used as a marker of regulatory T (Treg) cells. Briefly, a cell detection algorithm was trained to detect DAB-positive cells with nuclear area between 20 and 220 μm^2 and minimal roundness of 0.702 to enrich for lymphocytes and exclude stellate, spindle, and epithelial cells. FOXP3$^+$ lymphocytes were quantified in the DLP stroma as number of cells per unit area. The Mann–Whitney *U* test was used to determine differences in FOXP3$^+$ lymphocytes density in DLP stroma tissue sections from MYC mice fed an HFD or CTD.

Duplex ISH

The RNAscope 2.5 HD Duplex Chromogenic Assay was performed using the unique and validated RNAscope probes for *Mm-Adgre 1* (ACD, #460651, lot: 23130B) and *Mm-Cd274-C2* (ACD, #420501-C2, lot: 23130D), RNAscope 2.5 HD Duplex Detection Kit (ACD, #322430), and the HybEZ Hybridization System. Sample preparation (i.e., deparaffination, antigen retrieval, etc.) and assay were carefully performed as described by the manufacturer. Cells were counterstained using 50% hematoxylin-staining solution (Gill's hematoxylin I, Sigma-Aldrich, #GHS132) and 0.02% ammonia water for bluing step. Slides were mounted using the VectaMount mounting medium (Vector laboratories, #H-5000). Double-positive cells were counted in an area of 0.76 mm^2 by a board-certified MD Pathologist (P. Chetta). The Pathologist was blind to diet/genotype conditions. Images had been acquired using the Nano Zoomer-SQ image scanner system (Hamamatsu).

Metabolic profiling

Metabolic profiling in serum and DLP tissues was performed by LC/MS using Metabolon Inc. platform, similarly to Labbé and colleagues (15) and as briefly described.

Sample preparation

Biological samples were stored at −80°C and thawed on ice before extraction. Each sample was assigned a unique identifier using the Laboratory Information Management System (LIMS) to track all sample handling, tasks, and results. Tissue samples were weighed on a 4-position analytical scale (1/10th mg) and then soaked overnight in 80% methanol/20% deionized water with recovery standards at a 60 μL/1 mg ratio. Four recovery standards (DL-2-fluorophenylglycine, tridecanoic acid, d6-cholesterol and 4-chlorophenylalanine) were included in the methanol solution to assess metabolite extraction efficiency. For serum, 100 μL of sample was extracted with 500 μL of methanol containing the recovery standards. To remove proteins, dissociate small molecules bound to proteins or trapped in the precipitated protein matrix, and to recover chemically diverse metabolites, proteins were precipitated with methanol under vigorous shaking for 2 minutes (Glen Mills GenoGrinder 2000), followed by centrifugation. The resulting extract was divided in five fractions: two aliquots were used for two separate reverse phase (RP)/ultra-performance liquid chromatography/MS-MS (UPLC/MS-MS) methods with positive ion mode electrospray ionization (ESI), one aliquot was used for RP/UPLC/MS-MS with negative ion mode ESI, one aliquot was used for hydrophilic interaction LC/MS-MS (HILIC/UPLC/MS-MS with negative ion mode ESI), and one final aliquot was reserved for backup.

UPLC method

We used a Waters ACQUITY UPLC, and a Thermo Fisher Scientific Q-Exactive high resolution/accurate mass spectrometer interfaced with a heated electrospray ionization (HESI-II) source and Orbitrap mass analyzer operated at 35,000 mass resolution. Sample extracts were dried and then reconstituted in solvents compatible with each of the four analyses. Each solvent contained a series of standards at fixed concentrations to ensure injection and chromatographic consistency. One aliquot was analyzed using acidic positive ion conditions, chromatographically optimized for more hydrophilic compounds. The extract was gradient eluted from a C18 column (Waters UPLC BEH C18–2.1×100 mm, 1.7 μm) using water and methanol, containing 0.05% perfluoropentanoic acid (PFPA) and 0.1% formic acid. A second aliquot was also analyzed using acidic positive ion conditions, but chromatographically optimized for more hydrophobic compounds. The extract was gradient eluted from the C18 column using methanol, acetonitrile, water, 0.05% PFPA and 0.01% formic acid and was operated at an overall higher organic content. The third aliquot was analyzed using basic negative ion optimized conditions and a separate dedicated C18 column. The basic extracts were gradient eluted from the column using methanol, water, and 6.5 mmol/L ammonium bicarbonate, pH 8. The fourth aliquot was analyzed via negative ionization following elution from a HILIC column (Waters UPLC BEH Amide 2.1×150 mm, 1.7 μm) using a gradient consisting of water and acetonitrile with 10 mmol/L ammonium formate, pH 10.8. The MS analysis alternated between MS and data-dependent MSn scans using dynamic exclusion. The scan range varied slighted between methods but covered 70–1,000 m/z with a scan speed of approximately 9 scans per second (alternating between MS and MS-MS scans). Mass calibration was performed as needed to maintain <5 ppm mass error for all standards monitored.

QA/QC

Several controls were analyzed together with experimental samples: (i) a pooled matrix sample, generated by combining 20 μl of each experimental sample (i.e., prostate or serum), was injected six times for each dataset and served as a technical replicate to assess process variability; (ii) five water aliquots were extracted and analyzed to serve as blank for artifact determination; (iii) a cocktail of internal standards, carefully chosen to not interfere with the measurement of endogenous compounds, was spiked into every analyzed sample to monitor instrument performance and was also used as a retention marker for chromatographic alignment (LC Neg: D7-glucose, d3-methionine, d3-leucine, d8-phenylalanine, d5-tryptophan, bromophenylalanine, d15-octanoic acid, d19-decanoic acid, d27-tretadecanoic acid, d35-octadecanoic acid, d2-eicosanoic acid; LC HILIC: D35-octadecanoic acid, d5-indole acetic acid, bromophenylalanine, d5-tryptophan, d4-tryrosine, d3-serine, d3-aspartic acid, d7-ornithine, d4-lysine; LC Pos: D7-glucose, d3-methionine, d3-leucine, d8-phenylalanine, d5-tryptophan, bromophenylalanine, d4-tryrosine, d5-indole acetic acid, d5-hippuric acid, amitriptyline, d9-progesterone, d4-dioctylphthalate).

Instrument variability was determined by calculating the median relative standard deviation (RSD) for the standards that were added to each sample before injection into the mass spectrometer. The QCed data were automatically organized into curated metabolic pathways and piped into a secure, cloud-based digital environment for further analysis using custom-built bioinformatics tools, providing detailed pathway annotation based on integration of literature and institutional knowledge. For QA/QC, pooled QC plasma replicates from study samples was used to determine endogenous biochemical variability by calculating the median RSD for all endogenous metabolites (i.e., non-instrument standards) present in 100% of the pooled matrix samples, with representative RSD = 10% across all biochemicals. Experimental samples were randomized across the platform run with QC samples spaced to avoid batch effects.

Data extraction, compound identification, and quantification

Metabolon has developed a chemocentric approach for peak detection and integration. The data output is a list of *m/z* ratios, retention indices (RI) and AUC values, as previously described (22). User specified criteria for peak detection included threshold for signal to noise ratio, area, and width. RSDs of peak area were determined for each internal and recovery standard to confirm extraction efficiency, instrument performance, column integrity, chromatography, and mass calibration. The biological datasets, including QC samples, were chromatographically aligned on the basis of a retention index that used internal standards assigned a fixed RI value. The RI of the experimental peak was determined by assuming a linear fit between flanking RI markers whose RI values are set. Peaks were matched against an in-house library of authentic standards and routinely detected unknown compounds specific to the respective method. More than 5,200 commercially available purified standard compounds have been acquired and registered into LIMS for analysis on all platforms for determination of their analytic characteristics. Compound identification was based on RI values, experimental precursor mass match to the library authentic standard within 10 ppm, and quality of MS-MS match. Compound identification was then manually reviewed, and hand curated by an analyst who approved or rejected each identification on the basis of the criteria above. Additional mass spectral entries have been created for structurally unnamed biochemicals, which have been identified by virtue of their recurrent nature (both chromatographic and mass spectral). Peaks were quantified using AUC.

Data processing

Each metabolite was scaled on the median. Only metabolites with less than one third of missing values in at least two groups were kept for

statistical analysis. In each group (six replicates), a missing metabolite was imputed with 0 when absent in at least four replicates, otherwise the metabolite was imputed using the *k*-nearest neighbor (*k*NN) algorithm with $k = 5$.

Data analysis

Principal component analysis (PCA) was used to visualize the metabolomic data. Two-way ANOVA was used to identify metabolic changes induced by MYC-independent of diet. The Unpaired *t* test was used for two-group comparison. Benjamini–Hochberg-based FDR was calculated to correct for multiple comparisons. Metabolite changes were considered for further investigation/validation if *P* value was <0.05 and FDR <0.15, consistent with our previous work (15). Data processing and analysis were performed in R. Heat map was generated using Morpheus by Broad Institute (RRID:SCR_017386; https://software.broadinstitute.org/morpheus/).

Metabolic assays and lactate measurements

Serum levels of IGF-1, metabolic hormones, and adipokines were measured using the Mouse IGF-1 Single Plex array (MIGF1–01–101) and the Mouse, Rat Metabolic Array (MRDMET) at Eve Technologies. Lactate levels in DLP and serum were assessed using nuclear magnetic resonance (NMR) spectroscopy and colorimetric assays, respectively. For the NMR analyses, polar metabolites were extracted from DLP tissues with standard procedures, before performing NMR spectroscopy. Briefly:

Metabolite extraction

Intact frozen DLP tissues were carefully weighted and transferred into a glass vial (borosilicate clear glass with black phenolic cap, Fisherbrand). Polar metabolites were extracted following these steps: (i) addition of ice-cold methanol (14 mL/g) and pure water (3 mL/g) to the tissue sample; (ii) sonication-based tissue homogenization (Misonix Microson Ultrasonic cell Disruptor XL2000); (iii) addition of ice-cold chloroform (14 mL/g) followed by thorough vortexing; (iv) final addition of pure water (7 mL/g), followed by vortexing, incubation on ice (15 minutes), centrifugation (15 minutes at 1,000 × *g*), and collection of the methanol/water phase containing polar metabolites; (vi) evaporation of polar solvents with the SpeedVac vacuum concentrator (Concentrator plus/Vacufuge plus, Eppendorf). To avoid phases contamination, the polar phase was not entirely collected. This was accounted for in the final calculation of lactate concentration. Finally, polar metabolites were resuspended in 520 μL NMR buffer [containing 150 mmol/L sodium phosphate at pH 7.4 in D_2O, and 0.1% w/w trimethylsilylpropanoic acid (TSP) as chemical shift reference ($\delta = 0$ ppm)], vortexed, and centrifuged at 12,000 × *g* for 5 minutes. Supernatant (500 μL) was then transferred into NMR tube.

NMR spectroscopy

One-dimensional proton (^{1}H)-NMR spectra were recorded at 300 K on a Bruker AVANCE III 500 spectrometer equipped with a 5-mm inverse triple resonance $^1H/^{13}C/^{15}N$ TXI probe and x, y, z gradient coils. A nuclear Overhauser effect spectroscopy (NOESY) experiment was acquired using the NOESY-presat pulse sequence (noesygppr1d) where water suppression is performed through presaturation. The relaxation delay was set to 4s, the mixing time to 10 ms, the acquisition time to 2.7s, and the spectral window to 20 ppm. 512 transients were acquired with 54518 data points. Transformed spectra were corrected for phase and baseline distortions using Topspin 3.6 (Bruker BioSpin) and calibrated to the signal of sodium TSP at 0.00 ppm. The signal of lactate at 1.33 ppm (doublet) and TSP at 0.00 ppm were fitted by combining a local baseline and Voigt functions based on the multiplicity of the NMR signal (23). Lactate concentration was calculated according to the equation described in ref. 24.

Metabolic assays

Serum lactate was measured with the BioVision colorimetric assay kit (#K607–100), following the manufacturer's instructions.

Glycolytic proton efflux rate (GlycoPER) in MYC-CaP cells was measured with the Seahorse XFe24 analyzer (Agilent Technologies), following the manufacturer's instructions with some modifications. Briefly, MYC-CaP cells were plated in 24-well Seahorse plate (20,000 cells/well) for 24 hours in DMEM low glucose (1g/L, Euroclone ECM0749L) supplemented with 10% FBS, 4 mmol/L glutamine, and antibiotics. One hour before assay, medium was changed to Seahorse medium (Agilent Technologies 103575–100 with the addition of 5 mmol/L glucose, 1 mmol/L pyruvate, 2 mmol/L glutamine). Cells were incubated without CO_2 for 1 hour at 37°C. Medium was then again replaced before analysis with the Seahorse XFe24 analyzer. Assay was performed using the standard protocol, adjusting the measurements as following: 3 basal measurements (8 min each: 3 min mix, 2 min wait, 3 min measure), 8 measurements after injection with 5% (final concentration/well) of HFD or CTD serum (8 min each: 3 min mix, 2 min wait, 3 min measure), 3 measurements after injection with 0.5 μmol/L (final concentration/well) of rotenone/antimycin A (8 min each: 3 min mix, 2 min wait, 3 min measure), and 5 measurements after injection with 50 mmol/L (final concentration/well) of 2-DG (8 min each: 3 min mix, 2 min wait, 3 min measure). PER, glycoPER, basal glycolysis, basal PER, compensatory glycolysis, and after 2-DG acidification were calculated. GlycoPER was normalized to protein content/sample. Proteins were measured using Micro BCA Protein Assay Kit (Thermo Fisher Scientific, #23235).

Bulk RNA-seq and gene set enrichment analysis

Frozen DLP lobes were pulverized using a Cryoprep Pulverizer (Covaris). Total RNA was extracted with the RNeasy Plus MiniKit (Qiagen, #73404). RNA-seq libraries were prepared from 50 ng of total purified RNA using the KAPA Biosystems RNA HyperPrep Kit with RiboErase (Roche, #08098140702). Before library preparation, RNA quality was checked with the Agilent Bioanalyzer to calculate RIN score and DV200. RNA samples with a RIN score >5 were fragmented at 94°C for 8 minutes according to the manufacturer's recommendation. Those with RIN <5 were fragmented at 85°C for 2 minutes. dsDNA libraries were quantified by Qubit fluorometer, Agilent TapeStation 2200, and RT-qPCR using the Kapa Biosystems library quantification kit (Roche, #07960298001), according to the manufacturer's protocols. Uniquely indexed libraries were pooled in equimolar ratio and sequenced on an Illumina NovaSeq 6000 with paired end 50 bp reads at the DFCI Molecular Biology Core Facility. A count matrix was estimated through pseudo-alignment with salmon (25) using mm39 ensembl 104 transcripts annotations, which were summarized at the gene level with the tximport R/Bioconductor package. Low count genes (<5 CPM) were filtered, and the remaining genes were normalized with the trimmed mean of *M* values method (26). A generalized linear model approach coupled with empirical Bayes moderation of standard errors and voom precision weights was used to identify differentially expressed genes between the selected contrasts (27, 28). Correction for multiple testing was done with the Benjamini–Hochberg method. The results from differential expression analysis were ranked by t-statistics. Ranked lists were tested for gene set enrichment. Gene set enrichment analysis

(GSEA; RRID:SCR_003199) was performed using a Monte Carlo adaptive multilevel splitting approach, implemented in the fgsea R package. Hallmark gene sets were obtained from the Broad Institute MsigDB database (h.all.v7.5.1.symbols). Gene sets with less than 15 and more than 1,500 genes were removed from the analysis. The enriched pathways were collapsed to maintain only independent ones using the function collapsePathways from fgsea. Heat map was generated using Morpheus by Broad Institute (RRID:SCR_017386; https://software.broadinstitute.org/morpheus/). The tumor-associated macrophage (TAM) and Treg murine gene signatures were derived from the literature (29, 30). The endothelial cell signature was derived from publicly available single-cell RNA-seq (scRNA-seq) data of murine prostate lobes from 24-week-old mice (31).

scRNA-seq analyses

Processed data from scRNA-seq data of lateral and dorsal prostate lobes of 24-week-old FVB mice were downloaded from GSE228945 (32) and used to perform single-cell data analysis using the Seurat package (version 5.0.1). Low-quality cells were excluded (<200 genes, >75% mitochondrial reads) before merging lateral and dorsal prostate samples. Gene expression levels were normalized and scaled for subsequent analysis. A total of 2,000 highly variable genes were generated to perform PCA before data integration using the IntegrateData function from Seurat and *K*-mean clustering. Cell subtypes were identified by matching each cluster-specific gene with marker genes reported in Graham and colleagues (32). AUCell package (version 1.21.2) was used to calculate a cell-based "glycolytic signature" AUC score [AUC estimates the proportion of genes in a gene set that are highly expressed (top 5%) in each cell; AUC threshold >0.2] and identify the cell subtypes expressing the signature. The "glycolytic signature" is composed of the leading-edge genes from the hallmark_glycolysis gene set that was enriched in the contrast HFD_MYC versus CTD_MYC from GSEA of bulk RNA-seq in DLP.

Estimation of immune cell type composition and tumor purity

The computational models seq-ImmuCC (http://218.4.234.74:3200/immune/) and murine Microenvironment Cell Population counter (mMCP)-counter (mMCPcounter R package, version 1.1.0) were used to infer the relative proportions and abundance of major immune cell types in mouse tissues from bulk RNA-seq data, respectively (33, 34). In human tissues, deconvolute_quantiseq function from the R package immunedeconv (version 2.0.4) was used to estimate immune cell content from microarray expression data (35). To assess tumor purity, ESTIMATE (ESTIMATE R package, version 3.0.13; ref. 36), and PUREE (available at https://puree.genome.sg; ref. 37) methods were used.

Western blotting and densitometry

Fresh-frozen murine tissues were pulverized (Cryoprep Pulvrizer, Covaris) and lysed on ice in RIPA buffer (20 mmol/L Tris-HCl pH 7.5, 150 mmol/L NaCl, 1 mmol/L EDTA, 1 mmol/L EGTA, 1% NP-40) with the addition of phosphatase and protease inhibitor cocktail tablets (Complete Mini, EDTA-free, Roche, #11836170001; PhosSTOP, Roche, #4906837001). Fresh-frozen MYC-CaP tumor allografts were minced on ice with stainless steel disposable scalpels (Thermo Fisher Scientific) and then homogenized in RIPA buffer (20 mmol/L Tris-HCl pH 7.5, 150 mmol/L NaCl, 1 mmol/L EDTA, 1% TRITON-X) supplemented with phosphatase and protease inhibitors (Pierce Protease and Phosphatase Inhibitor Mini Tablets, EDTA free, Thermo Fisher Scientific, #A32961) using a tissue grinder kit (Kontes). Protein lysates were quantified with Bradford protein assay (Bio-Rad, #500020) or Pierce Rapid Gold BCA Protein Assay (Thermo Fisher Scientific, # A53225). Equal amounts of protein (10–25 μg for DLP tissues, 30 μg for MYC-CaP allografts) were resolved on precast 4% to 20% or 10% Tris-Glycine polyacrylamide (PA) gels (Bio-Rad Laboratories, #4561096, Invitrogen, #XP04205BOX) or 10% custom-made gels using Acrylamide/Bis-acrylamide, 30% solution (Bio-Rad, #1610158) and APS (Bio-Rad, #1610700), and transferred using Trans-Blot(R) Turbo (tm) Mini Nitrocellulose Transfer Packs (Bio-Rad Laboratories, #1704158), following the manufacturer's procedures. Alternatively, proteins were transferred using standard wet blotting systems (Bio-Rad, #1703810), using nitrocellulose membranes (GE Healthcare, Cytiva RPN2020D). Membranes were probed overnight (4°C) with primary antibodies [AR (Abcam, #ab108341, RRID:AB_10865716, dilution 1:1,000); β-actin (CST, #4970S, RRID:AB_2223172, dilution 1:1,000); β-actin (CST, #3700S, RRID:AB_2242334, dilution 1:1,000); MYC (Abcam, #ab32072, RRID:AB_731658, dilution 1:1,000); GLUT-1 (Abcam, #ab115730, RRID:AB_10903230, dilution 1:1,000); HIF1α (CST, #14179S, RRID:AB_2622225, dilution 1:1,000); LDHA (CST, #2012S, RRID:AB_2137173, dilution 1:1,000); MCT-1 (Santa Cruz Technology, #sc-365501, RRID:AB_10841766, dilution 1:200); MCT-4 (Santa Cruz Technology, #sc-376140, RRID:AB_10992036, dilution 1:200); vinculin (Sigma-Aldrich, #V9131, RRID:AB_477629, dilution 1:5,000). Membranes were washes with 0.1% Tween-TBS (three times, 5 min/each) and probed with secondary antibodies [goat anti-rabbit IgG (H+L)–HRP conjugate, Bio-Rad, #1706515, RRID:AB_11125142 or goat-anti-mouse IgG (H+L)–HRP conjugate, Bio-Rad, #1721011, RRID:AB_11125936] for 1 hour at room temperature. Chemoluminescent signal was developed using Amersham ECL Western Blotting Detection Reagent (GE Healthcare, Cytiva #RPN2020D) or Clarity Western ECL Substrate (Bio-Rad #1705061) and detected using Chemiluminescent Detection films (Hyblot CL, Thomas Scientific, #E3018) or the Chemidoc imaging system (Bio-Rad). Densitometry was performed with ImageJ (RRID:SCR_003070) or ImageLab (Bio-Rad, https://www.bio-rad.com/en-us/product/image-lab-software?ID=KRE6P5E8Z). Results were normalized to β-actin or vinculin and expressed as arbitrary units. GraphPad Prism version 9.3.0 (RRID:SCR_002798) was used for statistics and graph preparation.

Tube formation and wound-healing assays

Both tube formation and wound-healing assays were performed using standard procedures with some modifications as briefly described.

Tube formation assay

Six-hundred thousand HUVEC cells were seeded in a 6-well plate. Twenty-four hours after seeding, calcein-AM (Life Technology, #C-3099) was added for 40 minutes. Cells were harvested in EBM medium supplemented with 5% FBS. Seven thousand cells/well were seeded in the angiogenesis μ-slide (Ibidi, #81506), previously coated with 10 μL/well of Growth Factor-Reduced Matrigel (Corning, #356231), in the presence of PBS or sodium lactate (2, 10 mmol/L, Sigma, #L7022), or Recombinant Human VEGF (50 ng/mL, Peprotech, #100–20). For experiments using the lactate FX11 (20 μmol/L) or the dual MCT-1/MCT-4 inhibitor syrosingopine (10 μmol/L) or DMSO, cells were pre-treated with the drugs or vehicle for 48 hours before seeding in the μ-slide. Cells were not treated with calcein-AM. Tubes were visualized in bright-field using the Olympus IX71 or CK2 inverted microscopes, following 10 or 12 hours of treatment as indicated. For each condition, the number of segments/field was measured using the Angiogenesis Analyzer, a toolset of ImageJ software (RRID:SCR_003070). Default settings and minimum object size of 10 pixels were used.

Wound-healing assay

For wound-healing assays with/without lactate, MYC-CaP cells were plated at 800,000 cells/well in a 24-well plate in fresh medium containing 10% FBS. Twenty-four hours later, a scratch was performed with a p200 tip, medium was aspirated, cells were washed with PBS, and fresh medium containing lactate (10 mmol/L) or PBS was added. For wound-healing assays with/without LDHA inhibitor FX11, MYC-CaP cells were plated at 950,000 cells/well in a 24-well plate in fresh medium containing 10% FBS. Twenty-four hours later, a scratch was performed with a p200 tip, medium was aspirated, cells were washed with PBS, and fresh medium containing FX11 (1 μmol/L) or DMSO was added. Two images/wound were taken at different time points (0–48 hours), using an Olympus IX71 inverted microscope (4X objective). Wound areas were measured using the Analysis Particles analyzer, a toolset of ImageJ software (RRID:SCR_003070). Statistical analysis and graphical representation of data were performed with GraphPad Prism version 9.3.0 (RRID:SCR_002798).

Single-cell migration

MYC-CaP cells were pretreated with lactate (10 mmol/L) or PBS for 72 hours, plated, and cultured overnight on fibronectin-coated (0.1 mg/mL, Sigma-Aldrich, #F0895) 5 kPa PA gels with or without lactate. PA gels were prepared according to the procedure described by Califano and Reinhart-King (38) with the following modification: Coupling of the extracellular matrix (ECM) protein was achieved by functionalizing the surface of the PA gels with Sulfo-SANPAH (50 mg/mL, Thermo Fisher Scientific, #22589) and 10 minutes UV exposure. The PA gels were then coupled with fibronectin for 1 hour at 4°C. Images were acquired every 20 minutes for 12 hours using a Zeiss Axiovert 7 inverted microscope equipped with a 20×/0.4 N.A. objective and a chamber kept at 37°C and 5% CO_2. The fraction of motile cells was calculated. A cell was defined as motile if the centroid moved over a distance of at least one cell diameter during a defined observation period. Cell migration was manually tracked by outlining the cells and calculating the displacement of the cell centroid with ImageJ software (RRID:SCR_003070). Cell migration was quantified over a short period (3 hours) to avoid track interruption due to cell division. The mean square displacement was then computed and further fitted using the previously reported random walk equation $\langle d^2 \rangle = 2S^2 P(t-P(1-e^{(-t/P)}))$, where S is the average cell speed and P the persistence time using a nonlinear least square regression analysis (39).

Traction force microscopy

Traction force microscopy (TFM) was performed using 5 kPa PA gels as previously described (40) with some modifications. Briefly, MYC-CaP cells were pretreated with lactate (10 mmol/L) or PBS for 72 hours. At the end of 72 hours, MYC-CaP cells were seeded on fibronectin-coated PA gels embedded with 0.5 μmol/L diameter fluorescent beads (Thermo Fisher Scientific, #F8812) and cultured overnight. The cell-seeded PA gels were then imaged on a Nikon TI2 inverted microscope equipped with an environmental chamber. The stress field resulting from individual cells traction forces was obtained by imaging the fluorescent beads beneath the cell. The unstressed bead field was then imaged following cell detachment with 0.25%, trypsin (for 10 minutes, at 37°C). Traction forces were computed using the established Fourier transform traction cytometry method as described before (41). Briefly, the cellular traction fields were computed using a custom code in MATLAB (MathWorks; RRID:SCR_001622) that solves the inverse problem in the Fourier space with Green's functions based on the bead displacements obtained from the stressed and unstressed images (computation details in 49). TFM data were log transformed before statistical analysis.

Human cohorts

Physicians' Health Study and the Health Professionals Follow-up Study

Previously described gene expression data from 319 patients with prostate cancer of the physicians' health study (PHS) and HPFS (Health Professionals Follow-up Study) prospective cohorts were used [Gene Expression Omnibus (GEO, RRID:SCR_005012) Series accession number GSE79021; refs. 15, 42]. For these patients, both gene expression data, fat intake, and body mass index (BMI) information were available. Stratification of patients according to saturated fat intake (SFI) and BMI has been previously described in refs. 15, 42. Patients with prostate cancer were considered very overweight/obese when BMI ≥ 27.5 and healthy weight (18.5 < BMI < 25). A mod.t.test (MKmisc_1.6 R package) was used to measure gene expression differences between patients with high SFI versus low SFI and to rank genes for GSEA. GSEA was performed using the clusterProfiler R package (version 3.18.1). Hallmark gene sets were obtained from the MSigDB database using the msigdbr package (version 7.5.1). Gene sets were considered enriched with an FDR adjustment of < 0.05. The leading-edge genes of the glycolysis gene set, which was enriched by SFI, were used as a signature to calculate a glycolytic score using the simpleScore function from Singscore R package (version 1.12.0). Patients with prostate cancer were categorized into high and low glycolytic groups based on the mean glycolytic score. Full description of patient characteristics and clinicopathological data, fat intake assessment, BMI, and gene expression profiling is provided in refs. 15, 42. Written informed consent was obtained from all participants. The studies were approved by the institutional review boards at the Harvard T.H. Chan School of Public Health and Partners Health Care, as described in refs. 15, 42.

TCGA/PRAD dataset

RNA-seq raw read counts and clinicopathological information from The Cancer Genome Atlas (TCGA)/prostate adenocarcinoma (PRAD) patients were downloaded from TCGA database (http://tcga-data.nci.nih.gov/tcga/; ref. 43) using the Bioconductor (RRID:SCR_006442) package TCGAbiolinks (version 2.14.1). Data from 488 patients with primary prostate cancer were used. Read count were then normalized for sequencing depth using the size factor method and transformed using the variance-stabilizing transformation (voom), both implemented in Deseq2 (RRID:SCR_015687) package (version 1.20.0). Data analysis and statistics were performed in R version 3.6.2 (2019-12-12). Patients were stratified on the basis of *LDHA* expression quartiles (4th quartile = high expression and the other 3 quartiles = other). Differences in patient disease-free survival between groups were estimated by the Kaplan–Meier survival analysis and log-rank tests. Differences in LDHA mRNA levels according to Gleason Score (GS) and recurrence status were calculated using the Mann–Whitney *U* test. Analyses were done using GraphPad Prism version 9.3.0 (RRID:SCR_002798).

META855 cohort

META855 consists of a multi-institutional and multiethnic cohort of 855 patients treated with radical prostatectomy with available transcriptomic, clinicopathological, and outcome data. Data were derived from five published studies that used the Decipher prostate genomic classifier test and included only patients who reached an undetectable PSA level after surgery, as previously described (44).

Microarray expression levels were normalized using the single-channel array normalization (SCAN) algorithm (SCAN.UPC R package, version 2.28.0). Multivariable analysis was performed using the Proportional Hazards Regression model by adjusting for the covariables seminal vesicle invasion, surgical margins, extracellular extension, age, preoperative PSA, and GS. A *P* value was calculated using the Wald test. Difference in *LDHA* mRNA levels between prostate cancer from patients with and without biochemical recurrence (BCR) was calculated with the Wilcoxon rank-sum test. Statistical analyses were performed using R (version 4.2.0).

Statistical analysis

Unless otherwise indicated, statistics and graphs were generated with GraphPad Prism version 9.3.0 (RRID:SCR_002798). A *P* value of <0.05 was considered statistically significant. Normal distribution (D'Agostino-Pearson omnibus normality test, Shapiro–Wilk normality test, Kolmogorov–Smirnov normality test) and equal variance (F test) were assessed before analysis using GraphPad Prism (RRID: SCR_002798). When assumptions were not met, nonparametric or unequal variance tests were used. For each statistical analysis, test name and whether is one- or two-sided is provided.

Data availability

Metabolomics, digital pathology, differential gene expression, and GSEA data are available as Supplementary Data Files. Murine RNA-seq data have been deposited in NCBI GEO (RRID: SCR_005012) and are accessible through GEO Series accession number GSE203139. scRNA-seq data used in this study are accessible through GEO Series accession numbers GSE165741 and GSE228945. Mass spectrometry spectra have been deposited in Metabolights and are accessible through accession number MTBLS3316 and MTBLS3317. NMR spectra are available in Github at https://github.com/tkcaccia/Lactate-quantification-by-NMR. Gene expression data from HPFS and PHS cohorts are available through GEO Series accession number GSE79021. TCGA/PRAD data are available from the TCGA database (http://tcga-data.nci.nih.gov/tcga/). META855 data are available through GEO Series accession numbers GSE62116, GSE72291, GSE79915, and GSE79957. The code that was generated to calculate the lactate concentration in DLP tissue from NMR spectra is available in the form of an R script at: https://github.com/tkcaccia/Lactate-quantification-by-NMR. All other raw data are available upon request from the corresponding authors.

Results

Obesogenic HFD accelerates the development of invasive prostate cancer

We compared 24-week-old Hi-MYC mice that overexpress the human c-MYC transgene in the prostate epithelium (hereafter referred to as MYC mice) and WT littermates fed either a lard-based HFD or CTD (**Fig. 1A**; refs. 15, 18). Mice fed an HFD, irrespective of their genotype, developed obesity-like features, including increased body weight (CTD group = 34.5 ± 5.8 g; HFD group = 45.0 ± 6.7 g), hyperglycemia (i.e., decreased circulating 1,5-anhydroglucitol), hyperinsulinemia, increased resistin, c-peptide, and amylin levels, decreased ghrelin levels as well as liver steatosis (Supplementary Fig. S1A–S1D; Supplementary Table S1). Untargeted metabolomics confirmed a distinct serum metabolic profile in mice fed an HFD with predominant changes in lipid species (154/290 metabolites altered by HFD were lipids, $P < 0.05$, FDR < 0.15, two-way ANOVA; Supplementary Fig. S1E; Supplementary Tables S2–S4). As MYC drives the transition from PIN to IA at 24 weeks (18), we used digital pathology to quantify the amount of benign epithelium, PIN, and IA in the three prostate lobes from mice fed an HFD or CTD. When present, IA was detected only in the DLP, despite the high expression of MYC transgene also in the ventral prostate (VP; **Fig. 1B**; Supplementary Fig. S2A and S2B). In the VP, we observed a significant increase in the average percentage of PIN in HFD_MYC mice (94%, range, 25%–100%, $n = 22$) vs. CTD_MYC mice (82%, range, 24%–100%, $n = 21$; $P = 0.0001$, Mann–Whitney test). In the DLP, we observed no difference in PIN penetrance (HFD_MYC: 84%, range, 49%–98%, $n = 24$; CTD_MYC: 74%, range, 13%–94%, $n = 21$; $P = 0.0859$, Mann–Whitney test; **Fig. 1C**). However, the incidence of IA was markedly increased in mice fed an HFD ($P = 0.0008$, Fisher exact test), confirming that HFD accelerates IA development (**Fig. 1D**; Supplementary Table S5). DLP from HFD_MYC mice also displayed increased areas of outgrowing protrusions, indicative of more advanced disease progression (HFD_MYC: average, 1.34 mm^2; range, 0.3–2.48 mm^2, $n = 24$; CTD_MYC: average, 0.68 mm^2; range, 0–1.95 mm^2, $n = 21$; $P = 0.0002$, Unpaired *t* test; **Fig. 1E**; Supplementary Table S5). Protein levels of androgen receptor (AR) or MYC transgene were not significantly altered by HFD; ruling out their direct role in accelerating IA development in mice fed an HFD (Supplementary Fig. S2C and S2D). No significant difference in proliferation rate (assessed as percentage of Ki-67^+ cells) was observed in DLP from mice fed either an HFD or CTD (Supplementary Fig. S2E). AP was minimally affected by PIN, independent of diet (HFD_MYC: 3%, range, 0%–13%, $n = 24$; CTD_MYC: 4%, range, 0%–14%, $n = 18$), consistent with the marginal expression of the MYC transgene in AP lobe at this time point (**Fig. 1C**; Supplementary Fig. S2A and S2B; Supplementary Table S5) and with our previous findings (45). HFD did not display any transforming effect on WT prostates (Supplementary Fig. S2F).

Altogether, these data support the notion that obesogenic HFD promotes aggressive prostate cancer without altering either AR or MYC transgene protein expression.

Obesogenic HFD amplifies MYC-driven metabolic reprogramming

Following the histopathology findings, we investigated the metabolic features of IA driven by MYC and by MYC/obesogenic HFD cooperation. Untargeted LC/MS-MS was performed in DLP from WT and MYC mice fed an HFD or CTD for 21 weeks. Six hundred and twenty-eight metabolites were detected and 603 analyzed after processing (Supplementary Tables S6–S8). PCA clearly separated DLP samples according to MYC expression. However, the MYC-transformed but not the WT prostate group was further subdivided by diet (**Fig. 2A**). These results are consistent with those we previously reported in younger mice (12-week-old; ref. 15), suggesting that HFD influences MYC-driven metabolic reprogramming at both early and advanced stages of tumorigenesis. MYC alters the levels of more than half of the metabolites analyzed compared with WT (392/603, $P < 0.05$, FDR < 0.15, two-way ANOVA; **Fig. 2B**), consistent with its role as a master metabolic regulator. In particular, MYC transformation promotes metabolic pathways that support cancer-enhanced anabolic and energetic requirements [e.g., FA synthesis/oxidation, amino acid metabolism, tricarboxylic acid (TCA) cycle, and glutaminolysis], increases the accumulation of metabolites implicated in methylation and polyamines synthesis (i.e., methionine, the methyl donor s-adenosyl methionine, and 5′-Methylthioadenosine), and boosts the uptake of inflammatory diet-derived FAs (i.e., polyunsaturated

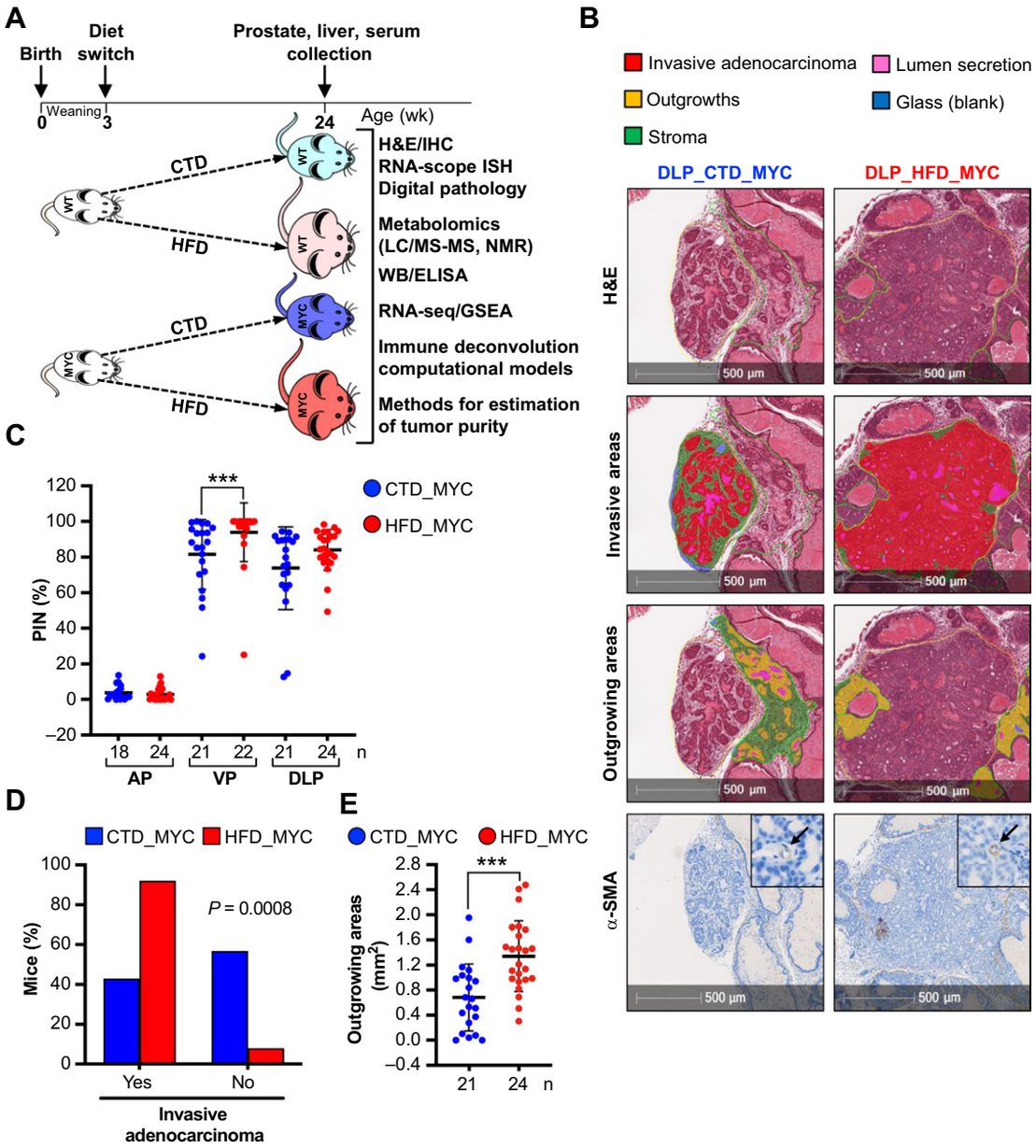

Figure 1.

Obesogenic high-fat diet accelerates the development of invasive adenocarcinoma. **A,** Experimental overview. **B,** Representative images of H&E (top), segmented invasive and outgrowing areas (middle), and a-smooth muscle actin (αSMA) IHC (bottom). The inset is a magnification of an area of invasive adenocarcinoma with complete negativity for αSMA. Black arrow, αSMA staining in vascular smooth muscle cells, which were used as internal positive control. Scale bar is shown. **C,** Dot plot showing the percentage of PIN in the whole lobe epithelium (benign + atypical). PIN percentage in anterior (AP), ventral (VP), and dorsolateral (DLP) prostate lobes was quantified using digital pathology (***, $P = 0.0001$, two-sided Mann–Whitney *U* test; *n*, biologically independent samples; mean ± SD). **D,** Bar plot showing the incidence of invasive adenocarcinoma. Data are presented as the percentage of MYC mice in each condition (CTD_MYC, $n = 21$; HFD_MYC, $n = 24$). A *P* value is shown (two-sided Fisher exact test). **E,** Dot plot comparing the size of outgrowing areas in DLP (***, $P = 0.0002$, two-sided unpaired *t* test; *n*, biologically independent samples; mean ± SD). ELISA, enzyme-linked immunoassay; ISH, *in situ* hybridization; WB, Western blotting.

arachidonic and linoleic acids; Supplementary Fig. S3A; Supplementary Table S8). HFD perturbs the metabolome of MYC-transformed prostate but only minimally affects WT prostate (**Fig. 2B**; Supplementary Fig. S3B and S3C; Supplementary Table S8). Of the 175 metabolites altered by HFD in MYC-transformed DLP, about two third were already increased by MYC and further augmented by HFD ($P < 0.05$, FDR < 0.15, Unpaired *t* test). These include intermediates of the synthesis of sarcosine, a putative biomarker of poor prognosis (46), glutaminolysis, TCA cycle, and branched-chain amino acid metabolism (**Fig. 2C**; Supplementary Table S8), suggesting that obesogenic HFD acts as a booster of MYC-driven metabolic dependencies.

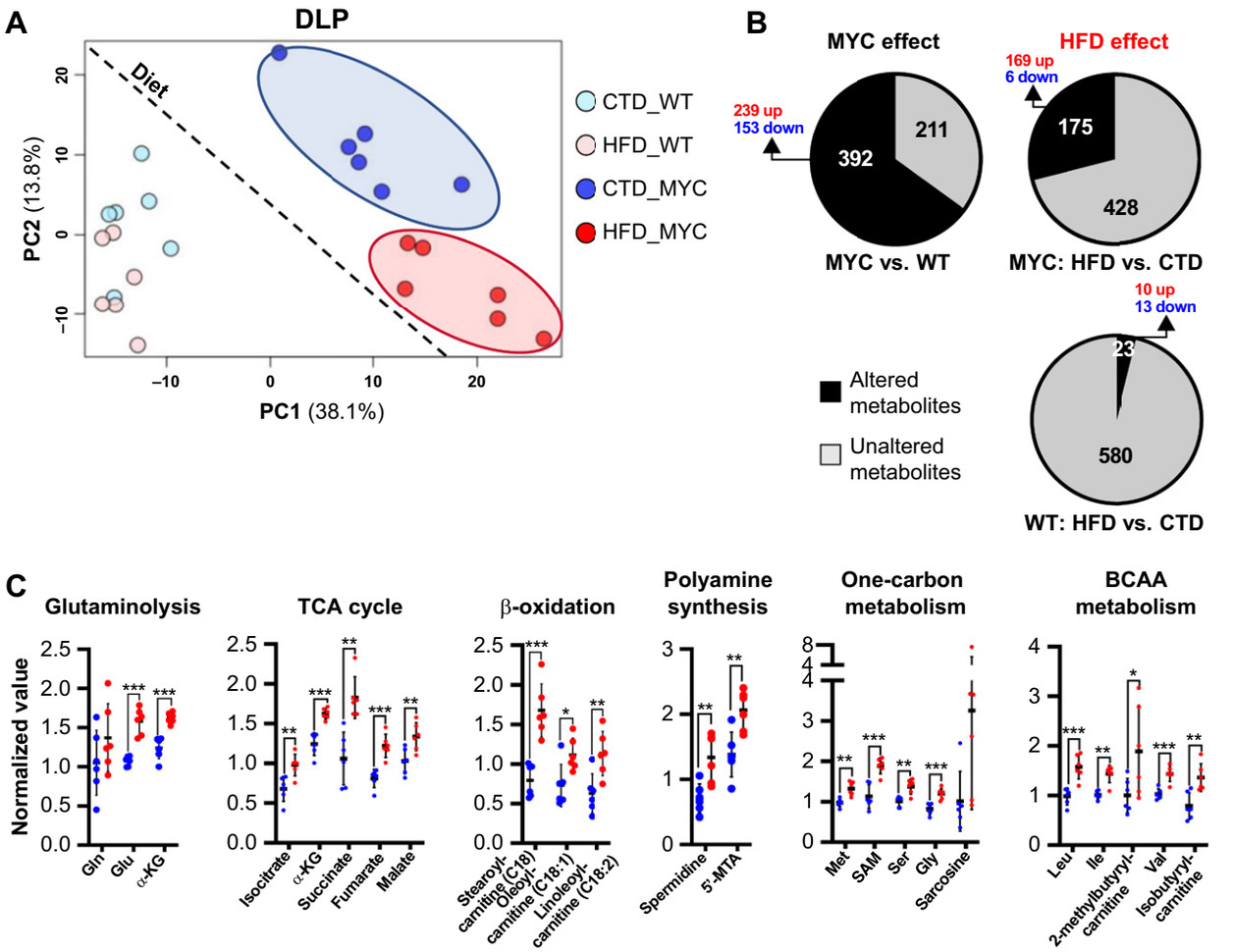

Figure 2.

Obesogenic high-fat diet amplifies critical MYC-dependent metabolic vulnerabilities. **A,** Principal component analysis of metabolomics data from DLP. Four diet/genotype conditions are represented ($n = 6$ biologically independent samples/group, 603 metabolites analyzed). **B,** Pie charts showing the proportion of metabolites significantly altered by MYC [MYC effect (independent of diet); $P < 0.05$, FDR < 0.15, two-way ANOVA] or by HFD in MYC-transformed or WT DLP (HFD effect; $P < 0.05$, FDR < 0.15, two-sided unpaired t test). **C,** Dot plots showing relevant metabolites of key pathways enhanced by HFD in MYC-transformed DLP ($P <$ 0.05; FDR < 0.15, two-sided unpaired t test; $n = 6$ biologically independent samples/group; mean ± SD). For each metabolite, comparison between HFD_MYC versus CTD_MYC is shown. *, $P < 0.05$; **, $P < 0.01$; ***, $P < 0.001$. Exact P and FDR values are summarized in Supplementary Table S8. αKG, α-ketoglutarate; BCAA, branched chain amino acids; Gln, glutamine; Glu, glutamate; Gly, glycine; Ile, isoleucine; Leu, leucine; 5-MTA, 5′-methylthioadenosine; Met, methionine; PC, principal component; SAM, s-adenosylmethionine; Ser, serine; Val, valine; WT, wild-type.

MYC cooperation with obesogenic HFD is required to promote lactate accumulation *in vivo*

To understand whether obesogenic HFD, beyond acting as a metabolic booster, also drives new metabolic liabilities in prostate cancer, we turned our attention to metabolites that were exclusively altered by MYC/HFD cooperation. Of the 46 significant metabolites ($P < 0.05$, FDR < 0.15, Unpaired t test) several are involved, as expected, in lipid metabolism. However, increased glucose-6-phosphate and lactate caught immediate attention (**Fig. 3A** and **B**; Supplementary Table S8) as prostate cancer commonly presents lipogenic/oxidative features. This suggests that the cooperation between HFD and genetic drive promotes a switch toward aerobic glycolysis (also known as Warburg effect) with the resulting accumulation of the oncometabolite lactate. A positive correlation between HFD-induced weight gain and intratumor lactate increase emerged (**Fig. 3C**, $R^2 = 0.5896$, $P = 0.0035$, Pearson correlation), whereas no change in serum lactate was observed (Supplementary Fig. S4A and S4B). NMR spectroscopy confirmed intratumor lactate accumulation in HFD-fed obese mice (**Fig. 3D**; Supplementary Table S9). Protein expression of LDHA, the enzyme responsible for the conversion of pyruvate to lactate, was significantly increased in DLP from MYC mice fed an HFD. HIF1α, a well-known inducer of aerobic glycolysis, was detected only in DLP from MYC mice fed an HFD (**Fig. 3E**; Supplementary Fig. S4C and S4D). However, lactate transporters (MCT-1 and MCT-4) protein levels were not changed (**Fig. 3E**; Supplementary Fig. S4E). HIF1α expression co-occurred with HFD-induced amplification of MYC transcriptional activity (**Fig. 3F**; Supplementary Table S10), suggesting their potential cooperation in promoting the Warburg effect, as previously described (47, 48).

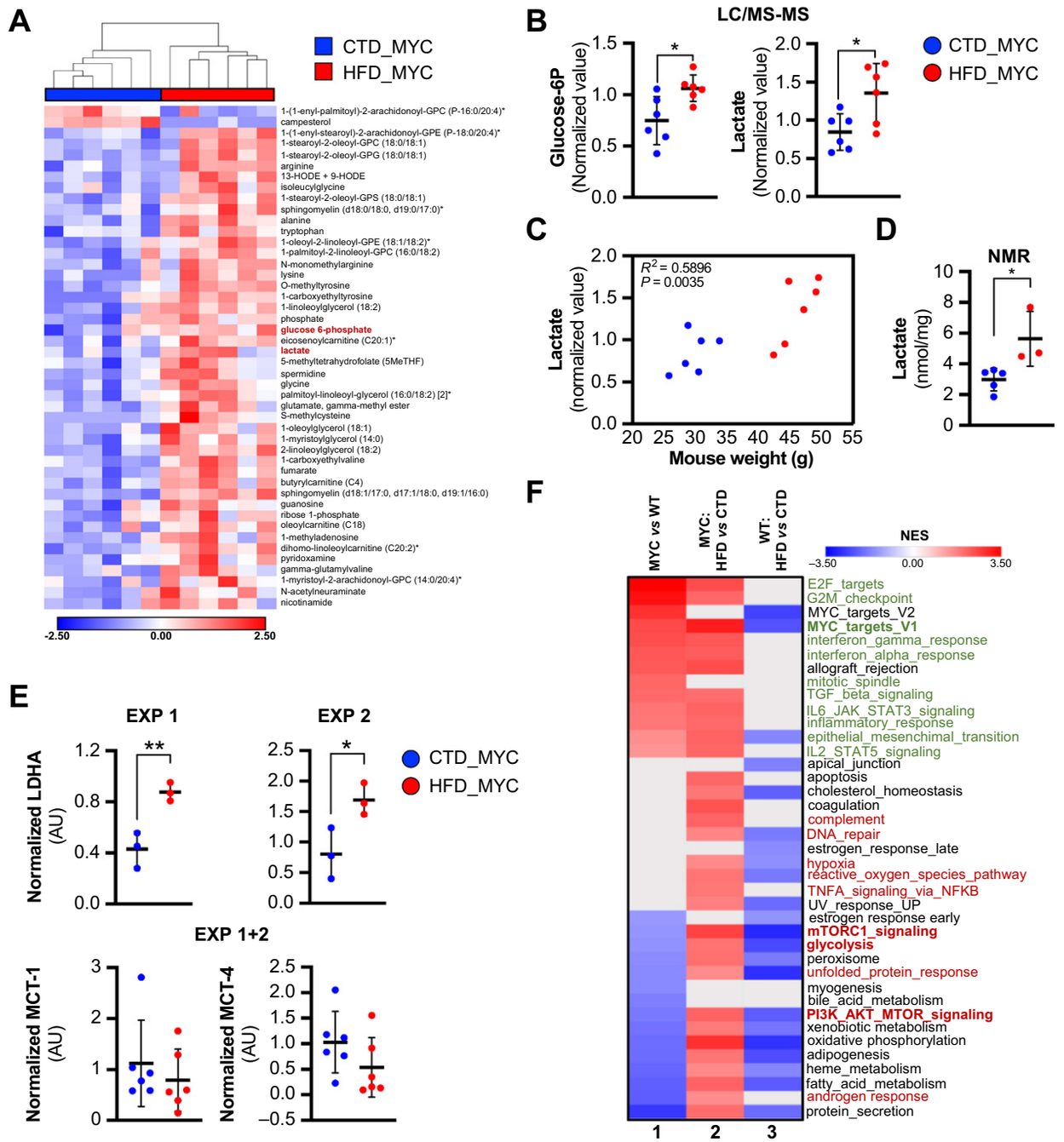

Figure 3.

Obesogenic high-fat diet promotes aerobic glycolysis in MYC-driven prostate cancer. **A,** Heat map showing the 46 metabolites that are uniquely altered by HFD in MYC-transformed DLP ($P < 0.05$; FDR < 0.15, two-sided unpaired *t* test; $n = 6$ biologically independent samples/group). Metabolite relative concentration, exact *P* and FDR values are summarized in Supplementary Table S8. Metabolites of aerobic glycolysis are highlighted in bold red. Metabolites were measured using LC/MS-MS. **B,** Relative quantification of glucose 6-phosphate (*, $P = 0.0211$) and lactate (*, $P = 0.0247$), two-sided unpaired *t* test; $n = 6$ biologically independent samples/group; mean ± SD. **C,** Association between mouse weight and lactate levels (Pearson correlation). Statistics are indicated. **D,** Lactate concentration in DLP using NMR (*, $P = 0.0227$, two-sided unpaired *t* test, $n = 3$–5 biologically independent samples). **E,** Western blot densitometric analysis of LDHA (EXP 1, **, $P = 0.0079$; EXP 2 and *, $P = 0.0358$, two-sided unpaired *t* test), MCT-1 ($P = 0.3939$, two-sided Mann–Whitney *U* test), and MCT-4 ($P = 0.1803$, two-sided unpaired *t* test); $n = 3$–6 biologically independent samples/group; mean ± SD. Protein levels are normalized to β-actin or vinculin and expressed as arbitrary units (AU). **F,** Heat map showing enriched/depleted gene sets in DLP (GSEA_Hallmark, $P < 0.01$; FDR < 0.01). Critical gene sets enriched by MYC and further enhanced by HFD are shown in green. MYC transcriptional activity is emphasized in bold green. Critical gene sets exclusively enriched in MYC-transformed DLP from mice fed HFD are marked in red. Glycolysis and related gene sets are further highlighted in bold red. Normalized enrichment scores (NES) are reported in Supplementary Table S10. WT, wild-type.

In line with metabolomics data, ^{18}F-FDG uptake was significantly increased in MYC-CaP allografts from mice fed an HFD. A parallel, though nonsignificant ($P = 0.0540$), increase in the glucose transporter GLUT-1 protein levels was also observed (**Fig. 4A–F**; Supplementary Table S11). Interestingly, the lactate exporter MCT-4 was expressed in allografts but not when MYC-CaP cells were grown *in vitro* under standard conditions or when supplemented with murine serum (Supplementary Fig. S4F). Seahorse analysis further confirmed that the exposure of MYC-CaP cells to murine serum from mice fed an HFD is not sufficient to promote aerobic glycolysis (Supplementary Fig. S4G), suggesting that an intact *in vivo* system is required to capture MYC/obesogenic HFD cooperation to promote a glycolytic switch and intratumor lactate accumulation.

Obesogenic HFD-induced transcriptional changes support the Warburg effect and disease progression

To gain further molecular insights, we performed bulk RNA-seq in DLP tissues (Supplementary Tables S12–S14). GSEA highlighted MYC/HFD cooperation in promoting transcriptional programs to support the Warburg effect and aggressive tumor features. Alongside the expected signatures associated with FA metabolism/oxidative phosphorylation, HFD was found to significantly enrich for glycolysis and glycolysis-associated gene sets (i.e., hallmark_glycolysis, hallmark_PI3K_AKT_mTORC1 signaling, hallmark_ mTORC1 signaling) in MYC-transformed DLP but not in the normal prostate (**Fig. 3F**, lanes 2 and 3; Supplementary Table S10). To rule out that the metabolic changes we observed were simply the results of HFD-induced changes in cellular composition rather than features of tumor metabolism rewiring, we estimated tumor purity and cell composition using the ESTIMATE and PUREE methods (36, 37). Neither method showed HFD-induced difference in tumor purity or stromal cell infiltration (Supplementary Fig. S5). Moreover, we leveraged scRNA-seq data from DLP of 24-week-old MYC mice (FVB, 32) and showed that the glycolytic signature (leading-edge genes of HFD-enriched hallmark_glycolysis gene set) was markedly expressed in the luminal cells, specifically in high Ly6d luminal subtype confirming that HFD-induced glycolytic shift affects epithelial tumor cells (Supplementary Fig. S6A–S6C). Gene sets related to MYC activity (i.e., MYC_targets_V1), cancer progression (i.e., epithelial to mesenchymal transition and TGFβ signaling), and inflammation (i.e., IFNγ and α response, IL6–JAK–STAT3 response) were all enriched in MYC-transformed prostate and further enhanced by HFD (**Fig. 3F**, lanes 1 and 2). However, MYC and HFD synergy was required to activate gene signatures of hypoxia, DNA repair, and AR transcriptional activity (i.e., androgen response; **Fig. 3F**, lane 2), the latter being significantly antagonized following MYC overexpression, as we described previously (45). Thus, not only does obesogenic HFD amplify the transcriptional effects of MYC-driven transformation, but it also cooperates with MYC to promote transcriptional changes that activate *ad hoc* metabolic programs and boost disease progression.

Obesogenic HFD modulates the TME

Intra-tumoral lactate accumulation has been reported to promote tumor cell migration, angiogenesis, and immune evasion, serving as fuel for lactate-avid Treg cells and as a stimulator of TAM M2 polarization (9, 49–52). Hence, we evaluated the effects of HFD/lactate accumulation on the TME. Deconvolution models based on bulk RNA-seq uncovered an increased proportion of infiltrating macrophages in MYC-transformed prostate from mice fed an HFD (**Fig. 5A**; Supplementary Fig. S7A and S7B). Concomitant enrichment of a pro-tumor (M2-like) TAM gene signature, previously derived from prostate-infiltrating macrophages of MYC mice, was detected (**Fig. 5B**; ref. 29). Not only did we validate the TAM signature in MYC-transformed DLP (Supplementary Table S15), but we also demonstrated further enrichment with HFD (**Fig. 5B**). Again, this feature was not observed in WT prostate (Supplementary Table S15). GSEA also uncovered enrichment of a gene signature related to tumor-infiltrating Treg cells in the DLP from MYC mice fed an HFD (**Fig. 5C**; Supplementary Table S15; ref. 30). Consistent with GSEA, IHC analysis confirmed increased infiltration of M2-like macrophages ($F4/80^+/CD206^+$) in the stroma of DLP from MYC mice fed an HFD. Furthermore, ISH analysis in a subset of cases showed a higher number of $F4/80^+/PD\text{-}L1^+$ macrophages in HFD_MYC DLP, confirming that HFD-promoted M2-like infiltrating macrophages display immune suppressive features (**Fig. 5D** and **E**). FOXP3 immunostaining and digital pathology were also used to quantify Treg in stromal areas of MYC-transformed DLP. A greater Treg cell density was detected in HFD-fed MYC mice both in the whole DLP stroma and in the peri-invasive stroma (**Fig. 5F** and **G**). In line with these findings, metabolomics uncovered HFD-mediated increased levels of kynurenine, an intermediate of tryptophan metabolism that mediates Treg cell generation/recruitment and effector T cells suppression (**Fig. 5H**; Supplementary Table S8; ref. 53). Taken together, our results demonstrate that obesogenic HFD/lactate accumulation promotes an immune suppressive TME to support prostate cancer progression.

Lactate promotes vascular tubulogenesis and prostate cancer cell motility

On the basis of our evidence for HFD-enhanced tumor invasiveness (**Fig. 1B–D**) and previous findings showing increased microvessel density in MYC mice fed an HFD (20), we leveraged an endothelial cell signature derived from a scRNA-seq dataset (31) and demonstrated the signature enrichment in HFD_MYC DLP (**Fig. 6A**) concurrent to increased protein expression of the angiogenic transcription factor HIF1α (Supplementary Fig. S4D). We then assessed whether HFD-induced intratumor lactate accumulation affect new vessel formation and prostate cancer cell migration using *in vitro* models directly exposed to lactate. MCT-1–expressing immortalized HUVEC (Supplementary Fig. S8A) and MYC-CaP cells were treated with high concentrations of lactate (2 and 10 mmol/L), which had been documented in human prostate cancer and other tumor types (54, 55). HUVEC treatment with lactate significantly increased the formation of capillary-like tubules on Matrigel (**Fig. 6B**). In contrast, inhibition of lactate synthesis or lactate uptake using the LDHA activity inhibitor FX11 (56) or the MCT-1/MCT-4 dual inhibitor syrosingopine significantly reduced tubulogenesis and prevented proper organization of capillary-like tubules on Matrigel, respectively (**Fig. 6C** and **D**). MYC-CaP cells treatment with lactate increased the fraction of motile cells, their displacement over time, and promoted collective cell migration (i.e., wound closure), without affecting cell proliferation (**Fig. 6E–G**; Supplementary Fig. S8B and S8C). In contrast, lactagenesis suppression with FX11 reduced MYC-CaP cell migration, without affecting either proliferation or LDHA/MCT-1 protein levels (**Fig. 6G**; Supplementary Fig. S8D–S8F). TFM revealed that MYC-CaP cells exerted higher traction forces on the ECM when exposed to lactate (Fig. S6H and S6I), in line with a more invasive phenotype (57). These results suggest that lactate accumulation contributes to enhance HFD-induced angiogenesis and tumor invasiveness.

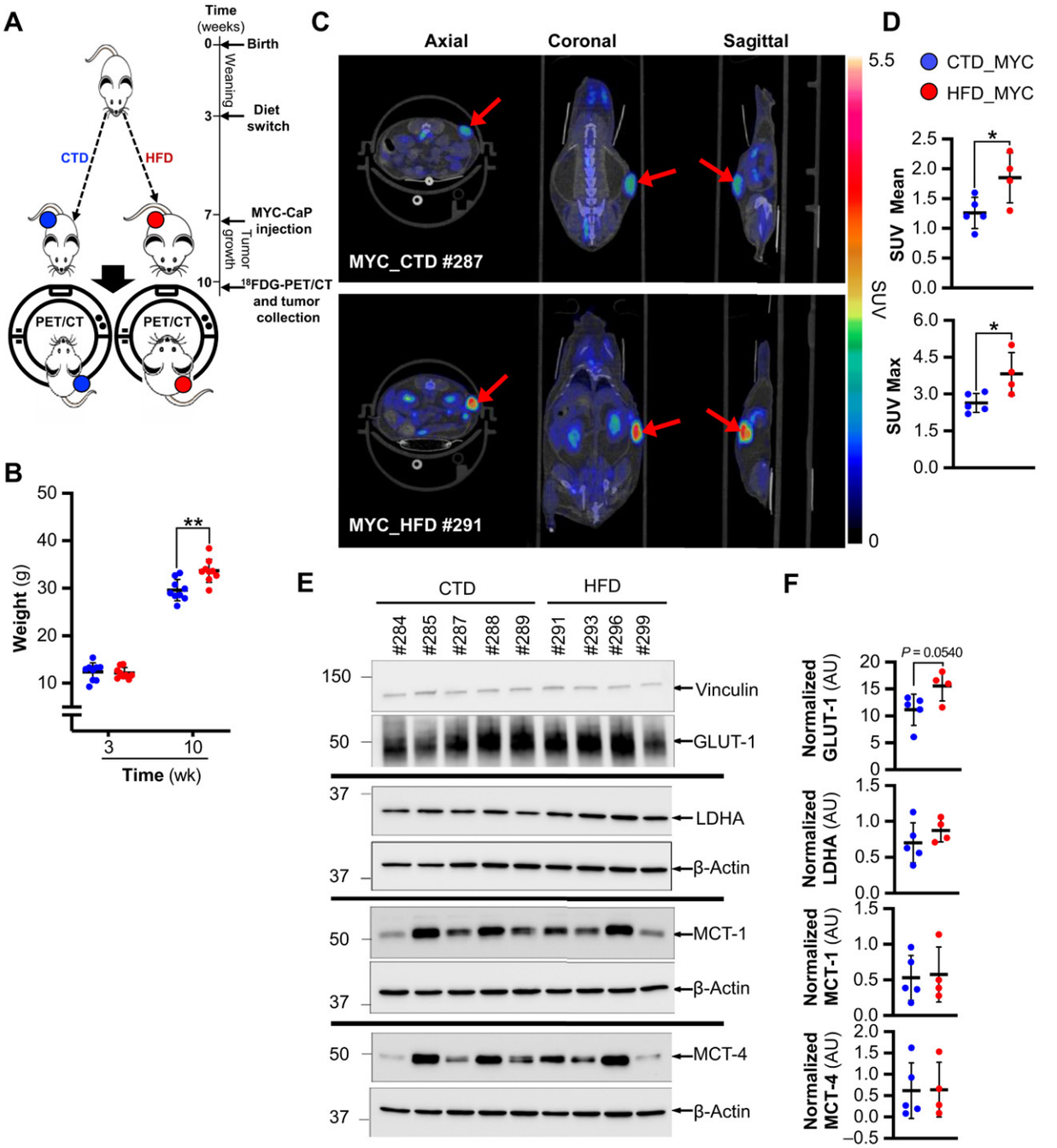

Figure 4.

Obesogenic high-fat diet boosts glucose uptake. **A,** Imaging experiment workflow. **B,** Mouse weight before the start of CTD/HFD feeding ($P = 0.7317$) and at the end of the study. **, $P = 0.0023$, two-sided unpaired t test; $n = 9$ mice/group; mean ± SD. **C,** Representative PET images (axial, coronal, and sagittal sections) of mice placed in prone position. **D,** Bar plots showing difference in mean (*, $P = 0.0355$) and maximum (*, $P = 0.0279$) SUV. Two-sided unpaired t test; $n = 4$–5 mice/group; mean ± SD. One mouse (HFD_MYC) with tumor volume unsuitable for PET analysis was excluded (see Materials and Methods). **E,** Western blot of GLUT-1, LDHA, MCT-1, and MCT-4 proteins. **F,** Densitometric analysis. Protein levels are normalized to β-actin or vinculin and expressed as arbitrary units (AU; GLUT-1, $P = 0.0540$; LDHA, $P = 0.3137$; MCT-1, $P = 0.8445$; MCT-4, $P = 0.9609$, two-sided unpaired t tests; $n = 4$–5 biologically independent samples/group; mean ± SD). ^{18}FDG-PET/CT, 2-deoxy-2-[18F]fluoro-D-glucose-PET/CT; GLUT-1, glucose transporter 1.

High saturated FA intake and BMI promote glycolytic features and TME modulation in human prostate cancer

Finally, we explored whether preclinical findings were recapitulated in the clinical setting. To do so, we used 319 primary prostate cancer and a subset of adjacent normal tissues ($n = 157$) from the HPFS and PHS prospective cohorts that we had previously stratified according to saturated FA intake and BMI (Supplementary Table S16; refs. 15, 42). In line with the preclinical data, patients with prostate cancer with high

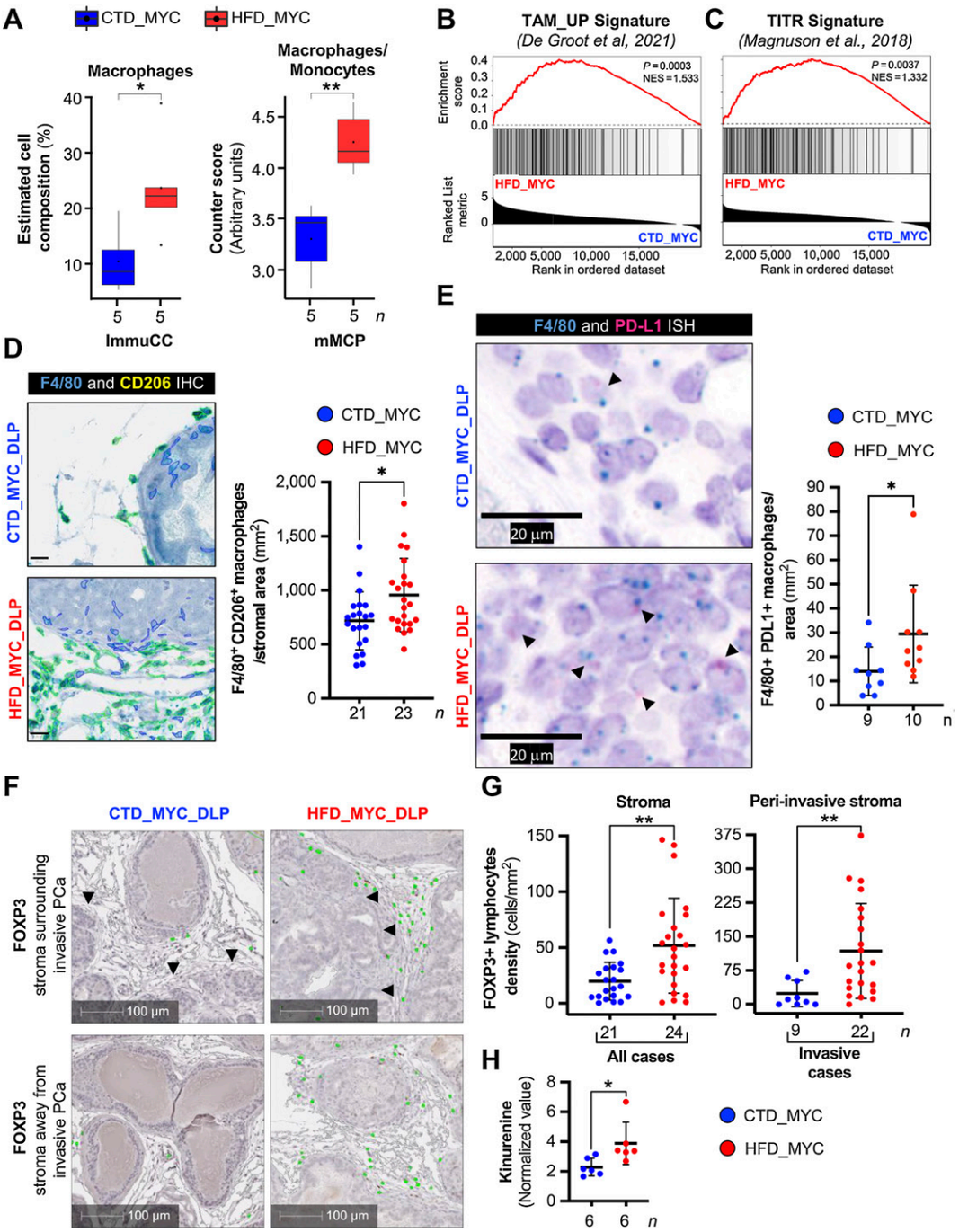

Figure 5.

Obesogenic high-fat diet promotes TAM and Treg infiltration in invasive prostate cancer. **A,** Box plots showing macrophage proportion using ImmuCC and mMCP deconvolution models (ImmuCC, *, $P = 0.016$; mMCP, **, $P = 0.0079$, two-sided Wilcoxon rank-sum test). Box plots show median value, box boundaries: 25th and 75th percentiles; interquartile range (IQR), whiskers: max or min value before the 1.5x IQR fence. The dot plotted in the IQR represents the mean value. **B** and **C,** Enrichment plot of TAM (**B**) and tumor-infiltrating Treg (TITR; **C**) signatures in MYC-transformed DLP. *P* value and normalized enrichment score (NES) are indicated. **D,** Left, representative images of F4/80 (teal) and CD206 (yellow) dual IHC staining in DLP stroma. Images show segmentation of double positive ($F4/80^+CD206^+$; green) and single positive ($F4/80^+$; blue) macrophages. Scale bar, 20 µm. Right, quantification (dot plot) of $F4/80^+CD206^+$ macrophages/stromal area in each case ($P = 0.0140$, two-sided unpaired *t* test). One case (HFD_MYC) was removed from the analysis due to a staining issue. **E,** Left, representative images of dual ISH with RNAscope probes for *Mm-Adgre1* (F4/80; teal) and *Mm-Cd274-C2* (PD-L1; red). Right, quantification (dot plot) of $F4/80^+PD\text{-}L1^+$ macrophages/area in each case ($P = 0.0260$, two-sided Mann–Whitney *U* test). Dual ISH was performed in a subset of cases. One case (CTD_MYC) was removed from the analysis due to a technical issue. **F,** Representative images of FOXP3 immunohistochemical staining in DLP stroma. $FOXP3^+$ lymphocytes are highlighted in green. Scale bar is shown. Black arrows, invasive glands. **G,** Quantification of $FOXP3^+$ lymphocytes using digital pathology. Data are expressed as number of $FOXP3^+$ lymphocytes/stromal area (left, $P = 0.0036$; right, $P = 0.0026$, two-sided Mann–Whitney *U* test). **H,** Dot plot showing kynurenine levels measured in DLP by LC-MS-MS (*, $P = 0.04$, FDR < 0.15, two-sided unpaired *t* test). In **D**, **E**, **G**, and **H**, data are expressed as mean ± SD; *n* = biological independent mice/group.

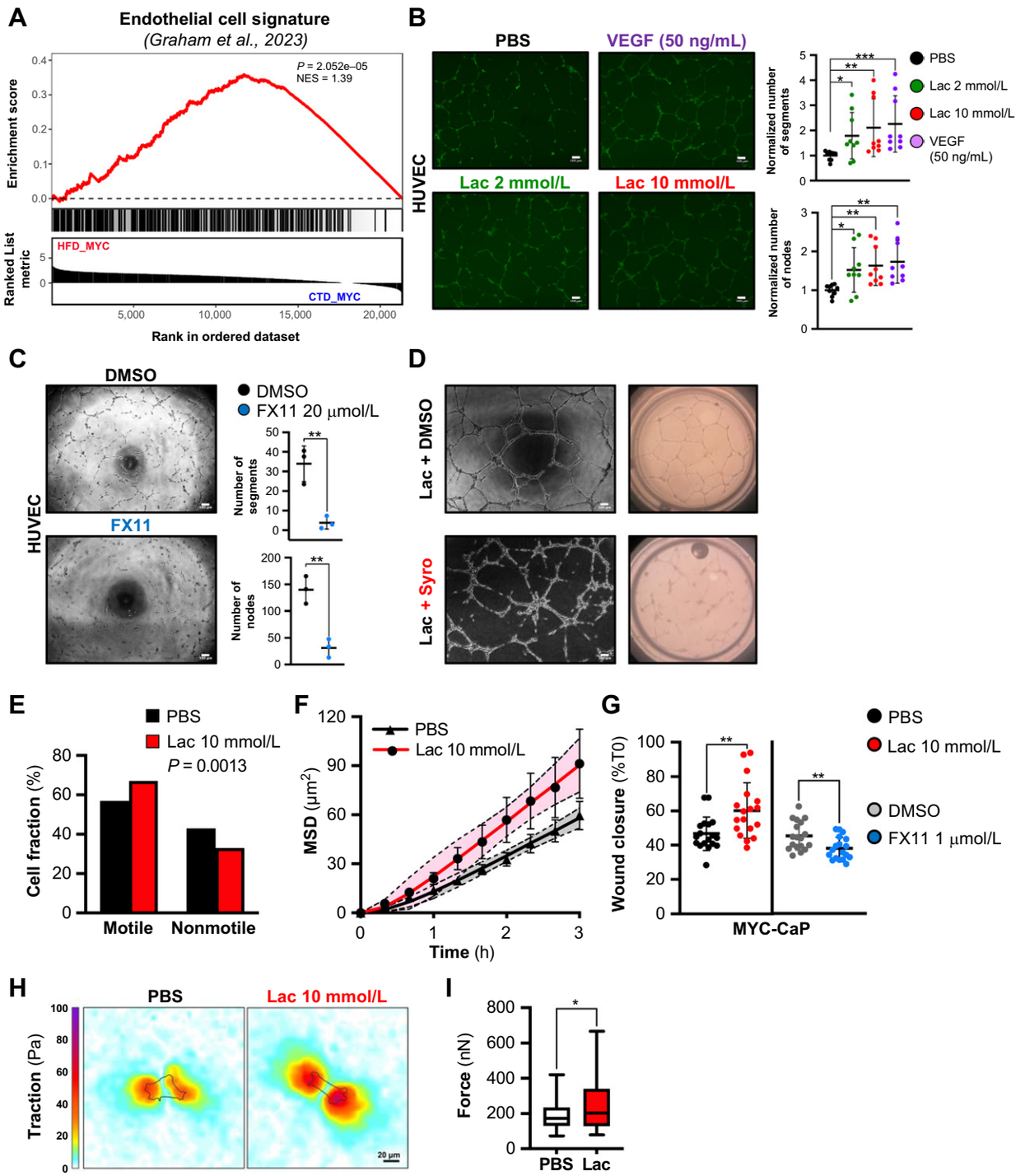

Figure 6.

Lactate promotes tubulogenesis and prostate cancer cell migration. **A,** Enrichment plot of an endothelial cell signature derived from scRNA-seq analysis of prostate lobes from 24-week-old mice. *P* value and NES are indicated. **B,** Tube formation assay. Left, representative pictures of HUVEC cells grown on Matrigel and stained with calcein AM green-fluorescent dye. Cells were treated for 12 hours with lactate or PBS. Treatment with VEGF was used as positive control. Scale bar, 100 µm. Right, quantification of tube segments and nodes (tube segments: *, $P = 0.0333$; **, $P = 0.0060$; VEGF, ***, $P = 0.0006$; tube nodes: *, $P = 0.0160$; **, $P = 0.0073$; VEGF, **, $P = 0.0014$, Kruskal–Wallis test). Number of segments and nodes in each well was normalized to the mean value of PBS condition in each experiment. Two independent experiments with three biological replicates; each was performed (two pictures/well were taken in EXP 1; one picture/well was taken in EXP 2, $n = 9$ pictures/group). **C,** Left, representative pictures of HUVEC cells grown on Matrigel in the presence of the LDHA inhibitor FX11 or DMSO for 10 hours. Scale bar, 100 µm. Right, quantification of tube segments and nodes (tube segments: **, $P = 0.0057$; tube nodes: **, $P = 0.0037$, two-sided unpaired *t* test). (*Continued on the following page.*)

saturated FA intake (SFI) showed higher BMI (**Fig. 7A**) and increased incidence of severely overweight/obese cases (about 35% and 15% in prostate cancer with high and low SFI, respectively, Supplementary Table S16). GSEA confirmed SFI-dependent enrichment of the glycolysis and glycolysis-promoting gene sets (i.e., hallmark_glycolysis, hallmark_mTORC1_signalling, hallmark_PI3K_AKT_MTOR_signalling) in prostate cancer but not in the adjacent normal tissue (**Fig. 7B**; Supplementary Table S17). The glycolysis gene set was not enriched by obesity *per se* (independent of FA intake) or by high SFI in lean patients, suggesting that high SFI with concomitant features of obesity is key in promoting the glycolytic switch (**Fig. 7C**, Supplementary Fig. S9A–S9C, Supplementary Tables S18–S19). Although these tumors had not been genetically characterized, prostate cancer from patients with high SFI bears enhanced MYC-transcriptional activity (MYC_targets_V1; Supplementary Table S17; ref. 15), in line with the preclinical data. Deconvolution models based on bulk RNA-seq uncovered a significant increased proportion of M2-like macrophages in highly glycolytic prostate cancer from patients with high SFI compared with low glycolytic prostate cancer or to prostate cancer from patients with low SFI (**Fig. 7D**, Supplementary Fig. S10). These data strongly suggest that prostate cancer acquisition of glycolytic features contributes to shaping a TME supportive of cancer progression.

To confirm that acquiring a "glycolytic phenotype" is associated with worse clinicopathological features, we interrogated both the TCGA/PRAD and META855 datasets (43, 44). High levels of *LDHA* were associated with increased GS, BCR, and shorter disease-free survival in the TCGA/PRAD dataset (**Fig. 7E–G**). The META855 dataset confirmed increased *LDHA* mRNA levels in BCR patients (**Fig. 7H**). Further multivariate analysis highlighted *LDHA* as independent predictor of BCR (**Fig. 8A**). Taken together, both preclinical and clinical data support the concept that obesogenic HFD, rich in saturated FAs, cooperates with oncogenic transformation to promote a tumor glycolytic switch that fosters prostate cancer progression (**Fig. 8B**).

Discussion

Prostate cancer represents the second cause of cancer-related death in men in the US and the third in Europe (10, 11). Although AR signaling is the major driver of the disease, evidence is accumulating that obesity and high consumption of saturated FAs contribute to the development of more advanced and lethal prostate cancer (12, 13, 42, 58). This is particularly worrisome in Western countries where prostate cancer incidence is rising and both obesity and consumption of unhealthy diets are increasing at alarming rates. The resulting socioeconomic impact is dramatic, highlighting the urgent need of improving therapeutic strategies and patient management (59).

Here, we explored whether the cooperation between obesogenic HFD and prostate cancer genetic drive (i.e., MYC overexpression) orchestrates specific metabolic programs that shape TME and support prostate cancer progression with the goal to identify new approaches of personalized nutrition and/or therapies targeting metabolic liabilities. In contrast to the ketogenic diet, characterized by very high fat and extremely low carbohydrate contents, our HFD, providing high fat but also carbohydrate intake, better resembles the western diet, which is associated with increased risk of obesity and obesity-like metabolic features in humans (60).

Digital pathology analyses demonstrated that obesogenic HFD accelerates MYC-driven IA development. However, unlike Blando and colleagues (20), we report IA only in DLP. This is relevant because DLP is the lobe that most closely resembles the human prostate peripheral zone, where prostate cancer typically develops (61). The integration of mass-spectrometry, RNA-seq, and ^{18}FDG-PET imaging approaches revealed that accelerated tumor progression is supported by a metabolic shift toward aerobic glycolysis, which is fueled by obesogenic HFD. NMR confirmed that intratumor lactate accumulation is observed in MYC-transformed prostate from HFD-fed obese mice, suggesting that obesity-associated hyperinsulinemia and hyperglycemia support the glycolytic shift in the murine model. Though recognized as one of the hallmarks of cancer, increased aerobic glycolysis or Warburg effect has not been a Leitmotiv in prostate cancer, whose classic features are increased oxidative metabolism and a lipogenic phenotype (62). However, imaging studies with hyperpolarized ^{13}C-MR (HP-MR) spectrometry have recently shown lactate accumulation in high-grade and castration-resistant prostate cancer. This is compelling that aerobic glycolysis and lactate accumulation indeed sustain prostate cancer aggressiveness and may represent a therapeutic target in advanced prostate cancer (55, 62–66). Our study fully aligns with and adds to these findings by showing that obesogenic HFD alters nutrient availability and tumor metabolic dependencies to boost prostate cancer progression. In an HFD-induced glucose- and insulin-enriched environment, transformed prostate cancer cells, but not their benign counterparts, become glucose-avid, enhance aerobic glycolysis, and ultimately accumulate lactate. Despite MCT are shared transporters for both lactate and ketone bodies (i.e., 3-beta-hydroxybutyrate), we did not observe alterations in ketone metabolism in our model. No glycolytic shift was observed when MYC-CaP cells in 2D were exposed to HFD serum, highlighting the concerted involvement of systemic metabolism and TME in MYC/HFD cooperation. Leveraging scRNA-seq data and deconvolution methods, we demonstrated that the glycolytic switch is not the result of HFD-induced changes in tumor purity and it affects mostly luminal cells, in particular luminal cells expressing Ly6d, a marker of castration resistance (67). Both metabolomics and transcriptomics data confirmed that MYC and HFD work as partners in crime. Prior events of oncogenic transformation are required for HFD to promote *ad hoc* metabolic (e.g., lactate accumulation) and transcriptional (e.g., hypoxia, androgen response) programs to promote disease progression. Recently, high lactate concentration has been associated to reduced sensitivity to

(*Continued.*) Experiment was performed with three biological replicates (each biological replicate was the average of 5 technical replicates). In **B** and **C,** mean values ± SD are shown. **D,** Left, representative pictures of HUVEC cells grown on Matrigel treated with MCT-1/MCT-4 dual inhibitor syrosingopine (Syro, 10 μmol/L) or DMSO in the presence of lactate 10 mmol/L for 12 hours. Scale bar, 100 μm. Magnifications, ×40 (right). Experiment was performed with two biological replicates (three technical replicates/each) and repeated twice. **E,** Bar plot showing the fraction of motile and non-motile cells under lactate or PBS treatment for 3 hours. Cells were previously pretreated for 72 hours. A *P* value is shown (two-sided Fisher exact test). Three independent experiments with three biological replicates were performed. **F,** Mean square displacement (MSD) overtime and matching nonlinear fits (95% CI; 301 cells/condition; mean ± SEM). **G,** MYC-CaP wound-healing assay. Bar plots showing the percentage of wound closure after 48 hours of treatment with lactate/PBS (**, $P = 0.0047$) or with FX11/DMSO (**, $P = 0.0058$), two-sided unpaired *t* test; mean ± SD. Three independent experiments with three biological replicates; each was performed. Two pictures/well were taken. **H,** Representative traction maps of MYC-CaP cells treated with lactate or PBS. Cell contour is shown (black line). **I,** Box plot showing average force in MYC-CaP cells treated with 10 mmol/L lactate ($n = 103$) or PBS ($n = 95$; *, $P = 0.0139$; two-sided unpaired *t* test with Welch correction). Box-plot shows median value, box boundaries: 25th and 75th percentiles; interquartile range, whiskers: min to max value. La, lactate; Pa, Pascal.

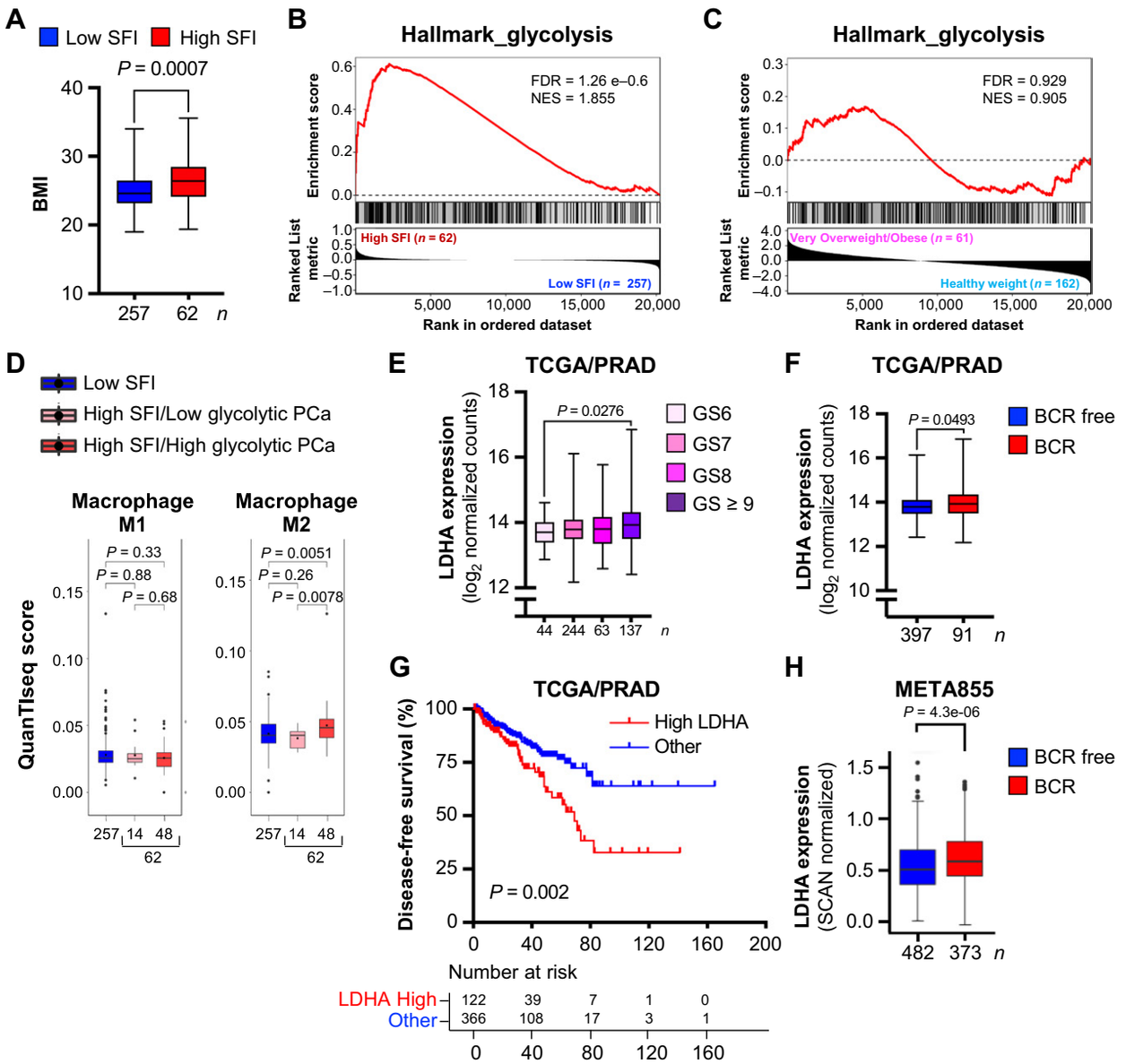

Figure 7.

High saturated fat intake and BMI are associated with prostate cancer tumors characterized by glycolytic features and an immunosuppressive TME. **A,** Comparison of BMI in prostate cancer patient with high and low SFI. **B** and **C,** Enrichment plot of "Hallmark_glycolysis" gene set in patients with prostate cancer stratified for SFI (**B**) and BMI (**C**). Normalized enrichment score (NES), FDR value, and number of cases are indicated. **D,** Box plots showing the proportion of tumor-infiltrating macrophages using QuanTIseq deconvolution model. Number of cases and *P* values are indicated. **E** and **F,** Box plots comparing LDHA mRNA levels in patients with prostate cancer with different Gleason score (GS; **E**) and BCR status (**F**). *P* values and number of patients are indicated; two-sided Mann–Whitney *U* test. Box plots show median value, box boundaries: 25th and 75th percentiles; interquartile range, whiskers: Min to max value. **G,** Kaplan–Meier curves of disease-free survival. A *P* value is indicated (log-rank test). **H,** Box plot comparing LDHA mRNA levels in patients with prostate cancer with/without BCR from the META855 dataset. For **D** and **H,** Wilcoxon rank-sum test was used; *P* value and number of patients are indicated. Box plots show median value, box boundaries: 25th and 75th percentiles; interquartile range (IQR), whiskers: max or min value before the 1.5x IQR fence. Dot plotted in the IQR represents the mean value. ns, not significant; PCa, prostate cancer.

enzalutamide (68), which is in line with our results of reactivation of AR signaling under HFD. Downplayed as a simple waste product for several decades, lactate has recently emerged as an "oncometabolite" involved in all the main aspects of cancer progression, including cell migration/invasion, angiogenesis, metastasis formation, epigenetic control, and immune escape (9). The mechanisms of immune evasion mediated by high levels of lactate include overexpression of the immune checkpoints PD-1 and PD-L1 on Treg and tumor cells, fueling of lactate-avid Treg cells, and polarization of macrophages toward an M2-like phenotype (49–51). Conversely, inhibiting

A

Multivariable analysis-biochemical recurrence

Variable	HR (95% CI)	*P*
Age	0.95 (0.94–0.96)	4.0643E–15
Preoperative PSA	1.00 (0.99–1.01)	4.7308E–01
Gleason score	1.53 (1.35–1.73)	1.0576E–11
Seminal vesicle invasion	1.44 (1.14–1.83)	2.1446E–03
Extracapsular extension	1.20 (0.97–1.50)	9.7082E–02
Surgical margins	1.52 (1.21–1.91)	3.2640E–04
LDHA (≦90 percentile)	Reference	
LDHA (>90 percentile)	**1.39 (1.02–1.90)**	**3.8824E–02**

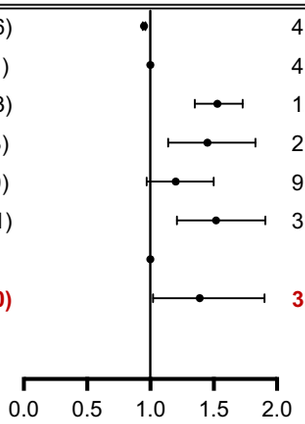

B

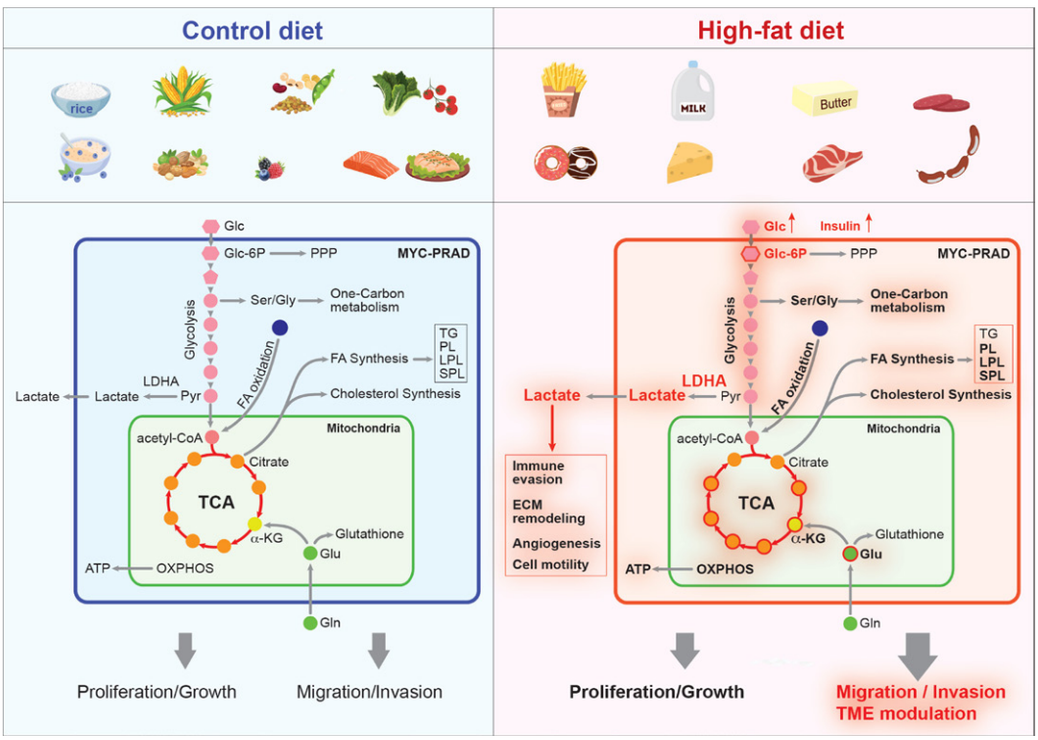

Figure 8.

Tumor acquisition of glycolytic features is associated with worse prognosis. **A,** Multivariable analysis (MVA) using the proportional hazards regression model. Hazard ratio (HR) ± 95% confidence interval (CI) is shown. The *P* value was calculated with the Wald test. **B,** Graphical summary. The oncogene MYC promotes a broad metabolic reprogramming. Obesogenic HFD not only enhances MYC-driven metabolic vulnerabilities (bold black) but also induces aerobic glycolysis and lactate accumulation (bold red). The latter boosts angiogenesis, ECM remodeling, prostate cancer cell migration, immune evasion, generating a TME permissive of prostate cancer progression. Red outline in hexagons/circles indicates metabolites that are increased with HFD in MYC-transformed DLP. αKG, α-ketoglutarate; $FADH_2$, flavin adenine dinucleotide; FA, fatty acid; Glc, glucose; Glu, glutamate; Gln, glutamine; LPL, lysophospholipid; OXPHOS, oxidative phosphorylation; NADH, nicotinamide adenine dinucleotide; PL, phospholipid; PPP, pentose phosphate pathway; Pyr, pyruvate; Ser/Gly: serine/glycine SPL, sphingolipid; TG, triglyceride. Of note, food images are not a direct translation of the murine diets used in this study.

enhanced lactate efflux from cancer cells preserves T cell effector functions and augments the effectiveness of immune checkpoint blockade (69). Physiologic levels of lactate can, however, directly fuel the TCA cycle, enhancing T-cell bioenergetic and biosynthetic capacity (70). This strongly highlights the crucial role of lactate in shaping immune cell phenotypes in both physiological and pathological conditions. Inflammation-related pathways (i.e., IFN gamma response, IFN alpha response, inflammatory response, TNFA signaling via NFKB, see **Fig. 3F**) were also enriched in prostate cancer from mice fed an HFD. Future studies using different dietary patterns and isocaloric diets will be required to better characterize the interplay with these inflammatory pathways. In this study, not only we confirmed that lactate boosts vascular tube formation (71), but we propose that this event may be part of an adaptative response to maintaining adequate nutrient and oxygen supply under hypoxia, which has emerged from GSEA of both HFD_MYC prostates and prostate cancer from patients with high SFI (**Fig. 3F**; Supplementary Table S17). We also demonstrated that lactate directly promotes prostate cancer cell migration and generation of higher traction forces on the underlying ECM, thus increasing prostate cancer cell contractility and ECM remodeling. The latter is crucial for cancer cell breaching through the basement membrane and for the release of chemoattractants and growth factors that promote neoangiogenesis and TME cell recruitment (72). We also proved that low concentration of FX11, which does not affect cell proliferation, is sufficient to inhibit prostate cancer cell migration, opening a therapeutic window for LDHA inhibitors to control disease progression without causing major side effects. Most relevant, this study uncovers a scenario whereby HFD-induced metabolic rewiring acts synergistically on both prostate cancer cells and TME to create a favorable *milieu* for invasive prostate cancer cells to thrive. Although accommodating oncogene-driven exacerbated anabolic and energetic needs of prostate cancer cells as the disease progresses, obesogenic HFD concurrently fosters an immunosuppressive TME through the intratumor accumulation of lactate. We indeed observed that both TAM M2-like ($F4/80^+$ $CD260^+$ and $F4/80^+$ $PD\text{-}L1^+$) and Treg ($FOXP3^+$) infiltration were significantly increase when lactate accumulates in IA from mice fed an HFD. These results are in line with recent observations whereby lactate secretion from PTEN/p53-deficient prostate cancer cells induces histone lactylation (H3K18lac) within macrophages and suppresses their phagocytic activity (73). Furthermore, our data suggest that formation of newly leaky vessels and increased cell contractility may contribute to lactate-induced TAM polarization and Treg infiltration. Further studies are, however, required to better clarify these aspects. Taken together, our preclinical findings bring forth the idea that pharmacological/dietary interventions aimed at reversing lactate accumulation represent potential means to overcome/delay resistance to standard of care treatments and improve response to immunotherapy, insofar largely ineffective in advanced prostate cancer. This is strongly supported by a recent study showing that reversal of lactate accumulation and PD-1–mediated TAM immunosuppression though a PI3K inhibitor and anti-PD1 antibody, respectively, improve the efficacy of androgen deprivation therapy (73). Inhibitors of LDHA and MCT are currently being developed or tested in clinical trials and they may be soon available for combinatory therapies (9).

Strikingly, preclinical findings translate into the clinical setting. Interrogating the prospective human cohorts HPFS and PHS we observed an increased BMI in patients with high-saturated FA intake and demonstrated that prostate cancer from these patients displays glycolytic features, in line with the results obtained in mice fed obesogenic HFD. This was associated with increased proportion of M2-like infiltrating macrophages, suggesting that prostate cancer acquisition of glycolytic features shapes the TME to support disease progression. Our results are consistent with recent evidence from scRNA-seq experiments in human metastatic prostate cancer samples, which revealed a direct correlation between tumor glycolytic activity and macrophage phagocytosis suppression (73). Obesity *per se* or high SFI in lean patients was not sufficient to induce tumor glycolytic features, suggesting that high SFI with concomitant features of obesity is key in promoting the glycolytic switch. It is also likely that obesity-associated modulation of hormonal axis and testosterone/estrogen levels might contribute to the prostate cancer metabolic rewiring.

Analysis of TCGA and META855 datasets further confirmed earlier evidence that acquiring a lactagenic phenotype, namely high levels of *LDHA* mRNA, is associated with more aggressive tumor features and worse prognosis (74), calling for clinical trials to test inhibitors of LDHA and lactate efflux in advanced prostate cancer. Recently, Sushentsev and colleagues (75) demonstrated the use of [1–^{13}C]pyruvate conversion to lactate HP-MR imaging as a biomarker predictive of clinically relevant disease, providing (i) a noninvasive approach to stratify high-risk patients and (ii) a potential tool to monitor response to LDHA and MCT-4 inhibitors. Our future work will specifically address this aspect.

In conclusion, this study identified lactate as a key mediator connecting obesogenic HFD, TME modulation, and prostate cancer progression, setting the stage for *ad hoc* dietary intervention (i.e., low saturated fat diet) and/or the use of lactagenesis inhibitors in advanced prostate cancer. Because intratumor lactate measurement is safely applicable in the clinic, this study strongly supports lactate assessment as both prognostic and predictive biomarker.

Authors' Disclosures

P.A. Sheridan reports personal fees from Metabolon during the conduct of the study. X. Zhao reports personal fees from Veracyte, Inc., during the conduct of the study; personal fees from Veracyte, Inc., outside the submitted work; and owns stock of Veracyte, Inc. Y. Liu reports personal fees from Veracyte, Inc., during the conduct of the study; personal fees from Veracyte, Inc., outside the submitted work; and owns stocks of Veracyte Inc. E. Davicioni reports personal fees from Veracyte, Inc., during the conduct of the study. D.E. Spratt reports personal fees from Astellas, AstraZeneca, Janssen, Pfizer, Novartis, Boston Scientific, and Bayer outside the submitted work. L.A. Mucci reports personal fees from Convergent Therapeutics and Bayer Pharmaceuticals, and grants from AstraZeneca outside the submitted work. L. Marchionni reports grants from NIH-NCI during the conduct of the study. D.P. Labbé reports other support from The Fonds de Recherche du Québec – Santé; grants from Canadian Institutes of Health Research, and grants and other support from Prostate Cancer Foundation during the conduct of the study. G. Zadra reports grants from US Department of Defense and World Cancer Research Fund (WCRF UK), as part of the World Cancer Research Fund International grant program during the conduct of the study. No disclosures were reported by the other authors.

Authors' Contributions

N. Boufaied: Conceptualization, formal analysis, investigation, visualization, writing–original draft, writing–review and editing, bioinformatics and statistical analyses. **P. Chetta:** Formal analysis, investigation, visualization, writing–original draft, writing–review and editing. **T. Hallal:** Investigation, writing–original draft, writing–review and editing. **S. Cacciatore:** Formal analysis, investigation, methodology, writing–review and editing. **D. Lalli:** Investigation, methodology, writing–review and editing. **C. Luthold:** Investigation. **K. Homsy:** Investigation. **E.L. Imada:** Formal analysis, murine RNA-seq analysis. **S. Syamala:** Investigation. **C. Photopoulos:** Investigation. **A. Di Matteo:** Investigation, writing–review and editing. **A. de Polo:** Investigation. **A.M. Storaci:** Investigation, writing–review and editing. **Y. Huang:** Investigation, immunohistochemistry. **F. Giunchi:** Investigation, Ki-67 IHC evaluation. **P.A. Sheridan:** Investigation, LC/MS-metabolomics. **G. Michelotti:** Investigation, writing–review and editing, scientific support in metabolomics. **Q.-De Nguyen:** Investigation, PET imaging experiments. **X. Zhao:** Formal

analysis, investigation, statistical analyses of human datasets. **Y. Liu:** Investigation, support in analysis of human datasets. **E. Davicioni:** Resources, support with analysis of human datasets. **D.E. Spratt:** Resources, support in analyses of human datasets. **S. Sabbioneda:** Resources. **G. Maga:** Resources. **L.A. Mucci:** Resources, writing–review and editing. **C. Ghigna:** Investigation, writing–review and editing. **L. Marchionni:** Investigation, supervision of murine RNA-seq analysis. **L.M. Butler:** Writing–review and editing, scientific support in data interpretation. **L. Ellis:** Resources, writing–review and editing, scientific/technical support. **F. Bordeleau:** Formal analysis, investigation, writing–review and editing. **M. Loda:** Resources, investigation, pathology support. **V. Vaira:** Resources, investigation, writing–review and editing. **D.P. Labbé:** Resources, supervision, funding acquisition, investigation, writing–original draft, project administration, writing–review and editing. **G. Zadra:** Conceptualization, resources, formal analysis, supervision, funding acquisition, investigation, visualization, writing–original draft, project administration, writing–review and editing.

Acknowledgments

T. Hallal is the recipient of the 100 Days across Canada Bursary Award. A. Di Matteo is supported by a fellowship from Fondazione Umberto Veronesi ETS. C. Ghigna is supported by an Investigator grant (IG-21966) from AIRC Foundation for Cancer Research. L.M. Butler is supported by a Principal Cancer Research fellowship produced with the financial and other support of Cancer Council SA's Beat Cancer Project on behalf of its donors and the State Government of South Australia through the Department of Health. F. Bordeleau is a Tier 2 Canada Research Chair in Tumor Mechanobiology and Cellular Mechanoregulation. D.P. Labbé is a William Dawson Scholar of McGill University, a Lewis Katz—Young Investigator of the Prostate Cancer Foundation and a Research Scholar—Junior 2 from The Fonds de Recherche du Québec – Santé. This study was supported by the Canadian Institutes of Health Research project grants (PJT-162246 to D.L. Labbé and PJT-180368 to F. Bordeleau and D.P. Labbé), the Idea Development Award from the US Department of Defense (PC150263 to G. Zadra), the Claudia Adams Barr Award in Innovative Basic Cancer Research from the Dana-Farber Cancer Institute (DFCI; to G. Zadra), and a grant (IIG_FULL_2022_020) funded from World Cancer Research Fund (WCRF UK) as part of the World Cancer Research Fund International grant program (to G. Zadra). The authors thank Prof. Myles Brown (DFCI) for his support with experimental models and contribution to some murine samples. We thank Zach Herbert, Andrew Caruso, Kristen Jones (DFCI), Anna Garbelli (CNR-IGM), Anna Maria Morotti, Marco Brevi, Prof. Stefano Ferrero (Division of Pathology, Fondazione IRCCS Ca' Granda Ospedale Maggiore Policlinico, Milan, Italy), Delfina Tosi (Department of Health Sciences, University of Milan, San Paolo Hospital, Milan, Italy), Monica Campagnoli and Prof. Ermanno Gherardi (Department of Molecular Medicine, University of Pavia, Italy), Fazila Chouiali (Histopathology platform, Research Institute of the McGill University Health Centre, Montréal, Québec, Canada) for technical assistance with RNA-seq, PET imaging, phase-contrast acquisition, IHC, and digital scanning. We thank Ericka M. Ebot (Harvard T.H. Chan School of Public Health, Boston, MA, currently at Foundation Medicine, Cambridge, MA), Meng Yang (Harvard T.H. Chan School of Public Health, Boston, MA, currently at Takeda, Cambridge, MA), and Jorge Chavarro (Harvard T.H. Chan School of Public Health, Boston, MA) for investigation of human cohorts, and Habiba El Fandy (DFCI, currently at Department of Pathology, National Cancer Institute, Cairo, Egypt) for pathology support. We thank Noriko Uetani for graphical summary design. We are grateful to Radha Kalekar (DFCI, currently at Brown University, Providence, RI), Debora L. Burkhart (DFCI), Kathryn Morel (DFCI, currently at South Australian Immunogenomics Cancer Institute, Adelaide, Australia), Carmen Priolo (Brigham and Women's Hospital, Boston, MA), Emmanuele Crespan and Chiara Mondello (CNR-IGM, Pavia, Italy), and Caroline Fidalgo Ribeiro (WCM, New York) for technical/experimental support and reagents. Finally, we would like to thank Profs. Mauro Botta and Mauro Patrone for the access to the NMR and biochemical facilities at University of Piemonte Orientale "A. Avogadro," Alessandria, Italy.

Note

Supplementary data for this article are available at Cancer Research Online (http://cancerres.aacrjournals.org/).

Received February 17, 2023; revised December 29, 2023; accepted April 5, 2024; published first June 4, 2024.

References

1. Bluher M. Obesity: global epidemiology and pathogenesis. Nat Rev Endocrinol 2019;15:288–98.
2. Lauby-Secretan B, Scoccianti C, Loomis D, Grosse Y, Bianchini F, Straif K, et al. Body fatness and cancer—viewpoint of the IARC working group. N Engl J Med 2016;375:794–8.
3. Goncalves MD, Hopkins BD, Cantley LC. Dietary fat and sugar in promoting cancer development and progression. Annual Review of Cancer Biology 2019;31:255–73.
4. Brandhorst S, Longo VD. Fasting and caloric restriction in cancer prevention and treatment. Recent Results Cancer Res 2016;207:241–66.
5. Anderson AS, Martin RM, Renehan AG, Cade J, Copson ER, Cross AJ, et al. Cancer survivorship, excess body fatness, and weight-loss intervention-where are we in 2020? Br J Cancer 2021;124:1057–65.
6. de Groot S, Lugtenberg RT, Cohen D, Welters MJP, Ehsan I, Vreeswijk MPG, et al. Fasting mimicking diet as an adjunct to neoadjuvant chemotherapy for breast cancer in the multicentre randomized phase 2 DIRECT trial. Nat Commun 2020;11:3083.
7. Vernieri C, Fuca G, Ligorio F, Huber V, Vingiani A, Iannelli F, et al. Fasting-mimicking diet is safe and reshapes metabolism and antitumor immunity in patients with cancer. Cancer Discov 2022;12:90–107.
8. Lyssiotis CA, Kimmelman AC. Metabolic interactions in the tumor microenvironment. Trends Cell Biol 2017;27:863–75.
9. Baltazar F, Afonso J, Costa M, Granja S. Lactate beyond a waste metabolite: metabolic affairs and signaling in malignancy. Front Oncol 2020;10:231.
10. Siegel RL, Miller KD, Fuchs HE, Jemal A. Cancer statistics, 2022. CA Cancer J Clin 2022;72:7–33.
11. Ferlay J, Colombet M, Soerjomataram I, Dyba T, Randi G, Bettio M, et al. Cancer incidence and mortality patterns in Europe: estimates for 40 countries and 25 major cancers in 2018. Eur J Cancer 2018;103:356–87.
12. Shirazipour CH, Freedland SJ. Obesity, visceral adiposity, and prostate cancer: What is the role of lifestyle interventions? Cancer 2019;125:2730–1.
13. Cao Y, Ma J. Body mass index, prostate cancer-specific mortality, and biochemical recurrence: a systematic review and meta-analysis. Cancer Prev Res 2011;4:486–501.
14. Lin PH, Freedland SJ. Dietary intake and prostate cancer, continued pursuit for evidence. Transl Androl Urol 2019;8:S246–S9.
15. Labbé DP, Zadra G, Yang M, Reyes JM, Lin CY, Cacciatore S, et al. High-fat diet fuels prostate cancer progression by rewiring the metabolome and amplifying the MYC program. Nat Commun 2019;10:4358.
16. Gurel B, Iwata T, Koh CM, Jenkins RB, Lan F, Van Dang C, et al. Nuclear MYC protein overexpression is an early alteration in human prostate carcinogenesis. Mod Pathol 2008;21:1156–67.
17. Sabnis HS, Somasagara RR, Bunting KD. Targeting MYC dependence by metabolic inhibitors in cancer. Genes 2017;8:114.
18. Ellwood-Yen K, Graeber TG, Wongvipat J, Iruela-Arispe ML, Zhang J, Matusik R, et al. Myc-driven murine prostate cancer shares molecular features with human prostate tumors. Cancer Cell 2003;4:223–38.
19. Nguyen QD, Perumal M, Waldman TA, Aboagye EO. Glucose metabolism measured by [(1)(8)F]fluorodeoxyglucose positron emission tomography is independent of PTEN/AKT status in human colon carcinoma cells. Transl Oncol 2011;4:241–8.
20. Blando J, Moore T, Hursting S, Jiang G, Saha A, Beltran L, et al. Dietary energy balance modulates prostate cancer progression in Hi-Myc mice. Cancer Prev Res 2011;4:2002–14.
21. Gertych A, Ing N, Ma Z, Fuchs TJ, Salman S, Mohanty S, et al. Machine learning approaches to analyze histological images of tissues from radical prostatectomies. Comput Med Imaging Graph 2015;46:197–208.
22. Dehaven CD, Evans AM, Dai H, L KA. Organization of GC/MS and LC/MS metabolomics data into chemical libraries. J Cheminform 2010;2:9.
23. Marshall I, Higinbotham J, Bruce S, Freise A. Use of voigt lineshape for quantification of *in vivo* 1H spectra. Magn Reson Med 1997;37:651–7.

24. Serkova N, Fuller TF, Klawitter J, Freise CE, Niemann CU. H-NMR-based metabolic signatures of mild and severe ischemia/reperfusion injury in rat kidney transplants. Kidney Int 2005;67:1142–51.
25. Patro R, Duggal G, Love MI, Irizarry RA, Kingsford C. Salmon provides fast and bias-aware quantification of transcript expression. Nat Methods 2017;14:417–9.
26. Robinson MD, Oshlack A. A scaling normalization method for differential expression analysis of RNA-seq data. Genome Biol 2010;11:R25.
27. Smyth GK. Linear models and empirical bayes methods for assessing differential expression in microarray experiments. Stat Appl Genet Mol Biol 2004;3:Article3.
28. Law CW, Chen Y, Shi W, Smyth GK. voom: precision weights unlock linear model analysis tools for RNA-seq read counts. Genome Biol 2014;15:R29.
29. de Groot AE, Myers KV, Krueger TEG, Kiemen AL, Nagy NH, Brame A, et al. Characterization of tumour-associated macrophages in prostate cancer transgenic mouse models. Prostate 2021;81:629–47.
30. Magnuson AM, Kiner E, Ergun A, Park JS, Asinovski N, Ortiz-Lopez A, et al. Identification and validation of a tumour-infiltrating Treg transcriptional signature conserved across species and tumour types. Proc Natl Acad Sci USA 2018; 115:E10672–E81.
31. Graham MK, Chikarmane R, Wang R, Vaghasia A, Gupta A, Zheng Q, et al. Single-cell atlas of epithelial and stromal cell heterogeneity by lobe and strain in the mouse prostate. Prostate 2023;83:286–303.
32. Graham MK, Wang R, Chikarmane R, Wodu B, Vaghasia A, Gupta A, et al. Convergent alterations in the tumor microenvironment of MYC-driven human and murine prostate cancer. bioRxiv 2023;17:2023.09.07.553268.
33. Chen Z, Quan L, Huang A, Zhao Q, Yuan Y, Yuan X, et al. seq-ImmuCC: cell-centric view of tissue transcriptome measuring cellular compositions of immune microenvironment from mouse RNA-seq data. Front Immunol 2018;9:1286.
34. Petitprez F, Levy S, Sun CM, Meylan M, Linhard C, Becht E, et al. The murine microenvironment cell population counter method to estimate abundance of tissue-infiltrating immune and stromal cell populations in murine samples using gene expression. Genome Med 2020;12:86.
35. Finotello F, Mayer C, Plattner C, Laschober G, Rieder D, Hackl H, et al. Molecular and pharmacological modulators of the tumour immune contexture revealed by deconvolution of RNA-seq data. Genome Med 2019;11:34.
36. Yoshihara K, Shahmoradgoli M, Martinez E, Vegesna R, Kim H, Torres-Garcia W, et al. Inferring tumour purity and stromal and immune cell admixture from expression data. Nat Commun 2013;4:2612.
37. Revkov E, Kulshrestha T, Sung KW, Skanderup AJ. PUREE: accurate pan-cancer tumor purity estimation from gene expression data. Commun Biol 2023;6:394.
38. Califano JP, Reinhart-King CA. The effects of substrate elasticity on endothelial cell network formation and traction force generation. Annu Int Conf IEEE Eng Med Biol Soc 2009;2009:3343–5.
39. Bordeleau F, Mason BN, Lollis EM, Mazzola M, Zanotelli MR, Somasegar S, et al. Matrix stiffening promotes a tumor vasculature phenotype. Proc Natl Acad Sci USA 2017;114:492–7.
40. Huynh J, Bordeleau F, Kraning-Rush CM, Reinhart-King CA. Substrate stiffness regulates PDGF-induced circular dorsal ruffle formation through MLCK. Cell Mol Bioeng 2013;6. doi: 10.1007/s12195-013-0278-7.
41. Mulligan JA, Bordeleau F, Reinhart-King CA, Adie SG. Traction force microscopy for noninvasive imaging of cell forces. Adv Exp Med Biol 2018;1092: 319–49.
42. Ebot EM, Gerke T, Labbé DP, Sinnott JA, Zadra G, Rider JR, et al. Gene expression profiling of prostate tissue identifies chromatin regulation as a potential link between obesity and lethal prostate cancer. Cancer 2017;123: 4130–8.
43. Cancer Genome Atlas Research N. The molecular taxonomy of primary prostate cancer. Cell 2015;163:1011–25.
44. Spratt DE, Yousefi K, Deheshi S, Ross AE, Den RB, Schaeffer EM, et al. Individual patient-level meta-analysis of the performance of the decipher genomic classifier in high-risk men after prostatectomy to predict development of metastatic disease. J Clin Oncol 2017;35:1991–8.
45. Qiu X, Boufaied N, Hallal T, Feit A, de Polo A, Luoma AM, et al. MYC drives aggressive prostate cancer by disrupting transcriptional pause release at androgen receptor targets. Nat Commun 2022;13:2559.
46. Sreekumar A, Poisson LM, Rajendiran TM, Khan AP, Cao Q, Yu J, et al. Metabolomic profiles delineate potential role for sarcosine in prostate cancer progression. Nature 2009;457:910–4.
47. Kim JW, Gao P, Liu YC, Semenza GL, Dang CV. Hypoxia-inducible factor 1 and dysregulated c-Myc cooperatively induce vascular endothelial growth factor and metabolic switches hexokinase 2 and pyruvate dehydrogenase kinase 1. Mol Cell Biol 2007;27:7381–93.
48. Dang CV. The interplay between MYC and HIF in the Warburg effect. Ernst Schering Found Symp Proc 2007:35–53.
49. San-Millan I, Brooks GA. Reexamining cancer metabolism: lactate production for carcinogenesis could be the purpose and explanation of the Warburg effect. Carcinogenesis 2017;38:119–33.
50. Watson MJ, Vignali PDA, Mullett SJ, Overacre-Delgoffe AE, Peralta RM, Grebinoski S, et al. Metabolic support of tumour-infiltrating regulatory T cells by lactic acid. Nature 2021;591:645–51.
51. Kumagai S, Koyama S, Itahashi K, Tanegashima T, Lin YT, Togashi Y, et al. Lactic acid promotes PD-1 expression in regulatory T cells in highly glycolytic tumour microenvironments. Cancer Cell 2022;40:201–18.
52. Noe JT, Rendon BE, Geller AE, Conroy LR, Morrissey SM, Young LEA, et al. Lactate supports a metabolic-epigenetic link in macrophage polarization. Sci Adv 2021;7:eabi8602.
53. Jennings MR, Munn D, Blazeck J. Immunosuppressive metabolites in tumoural immune evasion: redundancies, clinical efforts, and pathways forward. J Immunother Cancer 2021;9:e003013.
54. de la Cruz-Lopez KG, Castro-Munoz LJ, Reyes-Hernandez DO, Garcia-Carranca A, Manzo-Merino J. Lactate in the regulation of tumour microenvironment and therapeutic approaches. Front Oncol 2019;9:1143.
55. Sriram R, Van Criekinge M, DeLos Santos J, Ahamed F, Qin H, Nolley R, et al. Elevated tumour lactate and efflux in high-grade prostate cancer demonstrated by hyperpolarized (13)C magnetic resonance spectroscopy of prostate tissue slice cultures. Cancers 2020;12:537.
56. Le A, Cooper CR, Gouw AM, Dinavahi R, Maitra A, Deck LM, et al. Inhibition of lactate dehydrogenase a induces oxidative stress and inhibits tumour progression. Proc Natl Acad Sci USA 2010;107:2037–42.
57. Kraning-Rush CM, Califano JP, Reinhart-King CA. Cellular traction stresses increase with increasing metastatic potential. PLoS ONE 2012;7:e32572.
58. Van Blarigan EL, Kenfield SA, Yang M, Sesso HD, Ma J, Stampfer MJ, et al. Fat intake after prostate cancer diagnosis and mortality in the physicians' health study. Cancer Causes Control 2015;26:1117-.
59. Hecker J, Freijer K, Hiligsmann M, Evers S. Burden of disease study of overweight and obesity; the societal impact in terms of cost-of-illness and health-related quality of life. BMC Public Health 2022;22:46.
60. Clemente-Suarez VJ, Beltran-Velasco AI, Redondo-Florez L, Martin-Rodriguez A, Tornero-Aguilera JF. Global impacts of Western diet and its effects on metabolism and health: a narrative review. Nutrients 2023;15:2749.
61. Toivanen R, Shen MM. Prostate organogenesis: tissue induction, hormonal regulation, and cell type specification. Development 2017;144:1382–98.
62. Zadra G, Loda M. Metabolic vulnerabilities of prostate cancer: diagnostic and therapeutic opportunities. Cold Spring Harb Perspect Med 2018;8: a030569.
63. Bok R, Lee J, Sriram R, Keshari K, Sukumar S, Daneshmandi S, et al. The role of lactate metabolism in prostate cancer progression and metastases revealed by dual-agent hyperpolarized (13)C MRSI. Cancers 2019;11:257.
64. Granlund KL, Tee SS, Vargas HA, Lyashchenko SK, Reznik E, Fine S, et al. Hyperpolarized MRI of Human prostate cancer reveals increased lactate with tumour grade driven by monocarboxylate transporter 1. Cell Metab 2020;31: 105–14.
65. Pereira-Nunes A, Simoes-Sousa S, Pinheiro C, Miranda-Goncalves V, Granja S, Baltazar F. Targeting lactate production and efflux in prostate cancer. Biochim Biophys Acta Mol Basis Dis 2020;1866:165894.
66. Ippolito L, Comito G, Parri M, Iozzo M, Duatti A, Virgilio F, et al. Lactate rewires lipid metabolism and sustains a metabolic–epigenetic axis in prostate cancer. Cancer Res 2022;82:1267–82.
67. Barros-Silva JD, Linn DE, Steiner I, Guo G, Ali A, Pakula H, et al. Single-cell analysis identifies LY6D as a marker linking castration-resistant prostate luminal cells to prostate progenitors and cancer. Cell Rep 2018;25:3504–18.
68. Giafaglione JM, Crowell PD, Delcourt AML, Hashimoto T, Ha SM, Atmakuri A, et al. Prostate lineage-specific metabolism governs luminal differentiation and response to antiandrogen treatment. Nat Cell Biol 2023;25:1821–32.
69. Renner K, Bruss C, Schnell A, Koehl G, Becker HM, Fante M, et al. Restricting glycolysis preserves T-cell effector functions and augments checkpoint therapy. Cell Rep 2019;29:135–50.
70. Kaymak I, Luda KM, Duimstra LR, Ma EH, Longo J, Dahabieh MS, et al. Carbon source availability drives nutrient utilization in CD8(+) T cells. Cell Metab 2022; 34:1298–311.
71. Ruan GX, Kazlauskas A. Lactate engages receptor tyrosine kinases Axl, Tie2, and vascular endothelial growth factor receptor 2 to activate phosphoinositide 3-kinase/Akt and promote angiogenesis. J Biol Chem 2013;288:21161–72.

72. Winkler J, Abisoye-Ogunniyan A, Metcalf KJ, Werb Z. Concepts of extracellular matrix remodelling in tumour progression and metastasis. Nat Commun 2020; 11:5120.
73. Chaudagar K, Hieromnimon HM, Khurana R, Labadie B, Hirz T, Mei S, et al. Reversal of lactate and PD-1–mediated macrophage immunosuppression controls growth of PTEN/p53-deficient prostate cancer. Clin Cancer Res 2023; 29:1952–68.
74. Pertega-Gomes N, Felisbino S, Massie CE, Vizcaino JR, Coelho R, Sandi C, et al. A glycolytic phenotype is associated with prostate cancer progression and aggressiveness: a role for monocarboxylate transporters as metabolic targets for therapy. J Pathol 2015;236:517–30.
75. Sushentsev N, McLean MA, Warren AY, Benjamin AJV, Brodie C, Frary A, et al. Hyperpolarised ^{13}C-MRI identifies the emergence of a glycolytic cell population within intermediate-risk human prostate cancer. Nat Commun 2022;13:466.